A computational study on the energy efficiency of species production by single-pulse streamers in air

Baohong Guo, Jannis Teunissen*

Centrum Wiskunde & Informatica (CWI), Amsterdam, The Netherlands

E-mail: jannis.teunissen@cwi.nl

29 June 2023

Abstract. We study the energy efficiency of species production by streamer discharges with a single voltage pulse in atmospheric dry air, using a 2D axisymmetric fluid model. Sixty different positive streamers are simulated by varying the electrode geometry, the pulse duration and the applied voltage. Between these cases, the streamer radius and velocity vary by about an order of magnitude, but the variation in the maximal electric field is significantly smaller, about 30%. We find that G-values for the production of $N(^4S)$, $O(^3P)$, NO and N_2O, which have relatively high activation energies, vary by about 30% to 60%. This variation is mainly caused by two factors: differences in the fraction of energy deposited in the streamer head region, and differences in the maximal electric field at the streamer head. When accounting for both factors, our computed G-values are in good agreement with an analytic estimate proposed by Naidis (2012 *Plasma Sources Sci. Technol.* **21** 042001). We also simulate negative streamers and find that their production of $N(^4S)$, $O(^3P)$ and NO is less energy efficient. The results suggest that energy efficiency can be increased by reducing Joule heating in the streamer channel and by increasing the maximal electric field at the streamer head, for example by using short voltage pulses with a high applied voltage.

1. Introduction

Streamer discharges are fast-moving ionization fronts with self-organized field enhancement at their heads [1]. In such discharges, chemically active species are produced by collisions of energetic electrons with gas molecules [2]. Due to their highly non-equilibrium nature [3], streamer discharges can efficiently produce species with a high activation energy without significant gas heating. Streamer discharges are used for many plasma chemical applications such as air purification or ozone production [4–7], removal of nitrogen oxides [8–10], liquid treatment [11, 12], surface modification [13, 14], plasma medicine [15, 16] and plasma assisted combustion [17, 18].

In this paper, we computationally study how streamer properties affect the energy efficiency with which chemically active species are produced. Simulations are performed of both positive and negative streamers in atmospheric-pressure dry air, using a 2D axisymmetric fluid model. An advantage of simulations is that they contain information on all species densities and fields, and that discharge parameters such as the voltage waveform can easily be modified. However, it can be challenging to construct a suitable set of chemical reactions for given conditions and time scales of interest. We have here constructed a set of 263 chemical reactions primarily based on the reactions from [19–29], as shown in Appendix A.

Past work. Below, we briefly discuss some related computational and experimental work. Several authors have numerically studied the energy efficiency of species production in pulsed streamer discharges. This energy efficiency is often reported using G-values, in units of atoms or molecules produced per 100 eV of input energy. In simulations of positive streamers in air-methane [30], G-values for O and N radicals were found of about 0.7 and 1.5–1.7, respectively. It was observed that these G-values were relatively insensitive to the applied voltage and the streamer length. In [31], the authors simulated the production of $N_2(v=1)$, $O(^3P)$ and $N(^4S)$ in primary and secondary streamers in atmospheric-pressure dry air. When the applied voltage was increased, G-values for $O(^3P)$ increased and G-values for $N_2(v=1)$ decreased, since these species have different activation energies. In [32], G-values for the production of oxygen and nitrogen atoms in positive streamers in atmospheric air were computed, in sphere-plane gaps. It was observed that the calculated G-values weakly depended on the applied voltage and discharge conditions, which were found to be about 3–4 and 0.3–0.4 for oxygen and nitrogen atoms, respectively. An analytical estimate was made for the G-values of the production of chemically active species with high activation energies, which was further worked out in [33], as discussed in more detail in section 5.1.

We also give a few examples of relevant experimental work on the energy efficiency of NO-removal, which depends on the production of oxygen and nitrogen radicals. In [34], the greatest removal efficiency was found when pulsed positive corona discharges were generated with short high-voltage pulses. These pulses were shorter than the time required for primary streamers to bridge the discharge gap. In [35], the authors used pulsed discharges to remove NO in a mixture of N_2, O_2 and H_2O. They found the removal energy efficiency increased for shorter pulse widths. The influence of shorter pulse duration on NO-removal energy efficiency was also confirmed by [36], in which a high energy efficiency (0.43 mol/kWh) for NO-removal by nanosecond pulsed discharges was found. Relevant experimental work on the energy efficiency of O_3 production can be found in section 5.3.

2. Simulation model

We use a 2D axisymmetric drift-diffusion-reaction type fluid model with the local field approximation to simulate streamers in 80% N_2 and 20% O_2, at 300 K and 1 bar. Pulsed streamer discharges and their afterglows are simulated up to $t = 500$ ns using the open-source `Afivo-streamer` code [37].

2.1. Model equations

The temporal evolution of the electron density n_e is given by

$$\partial_t n_e = \nabla \cdot (\mu_e \mathbf{E} n_e + D_e \nabla n_e) + S_e + S_{ph}\,, \tag{1}$$

where μ_e is the electron mobility, $\mathbf{E}$ the electric field, D_e the electron diffusion coefficient. Furthermore, S_{ph} is the source term for non-local photoionization and S_e is the sum of electron source terms from the reactions listed in table A2. For photoionization, we use Zheleznyak's model [38] and the so-called Helmholtz approximation [39, 40], with the same parameters as in [41].

The temporal evolution of each ion species n_i ($i = 1, 2, \ldots, n$, listed in table 2) is given by

$$\partial_t n_i = -\nabla \cdot (\pm \mu_i \mathbf{E} n_i) + S_i\,, \tag{2}$$

where the $\pm$ accounts for the ion charge, μ_i the ion mobility, and S_i is the sum of ion source terms from the reactions listed in table A2. For simplicity, we use a constant ion mobility $\mu_i = 2.2 \times 10^{-4}\,\mathrm{m^2 V^{-1} s^{-1}}$ [23] for all ion species, as in [42, 43]. For O_2^+, the photoionization source term S_{ph} is included in S_i.

The electric field $\mathbf{E}$ is calculated as $\mathbf{E} = -\nabla\phi$. The electric potential ϕ is obtained by solving Poisson's equation

$$\nabla^2 \phi = -\rho/\varepsilon_0\,, \tag{3}$$

where ρ is the space charge density and ε_0 is the vacuum permittivity. Equation (3) is solved using the geometric multigrid method included in the Afivo library [44, 45].

2.2. Chemical reactions and input data

We have constructed a set of 263 chemical reactions, based on the reactions from [19, 29] with additional reactions primarily from [20–28]. A list of all 56 considered species is given in table 2. The complete reaction list is given in Appendix A, which also contains a list of the considered excited states of N_2 and O_2.

The transport coefficients μ_e and D_e, and reaction rate coefficients for reactions R1–R30 in table A2 are functions of the reduced electric field E/N, where E is the electric field and N is the gas number density. These coefficients were computed with BOLSIG+, a two-term electron Boltzmann equation solver [46], using the temporal growth model. Electron-neutral scattering cross sections for N_2 and O_2 were obtained from the Phelps database [47–49].

2.3. Computational domain and initial condition

The 2D axisymmetric computational domain used in the simulations is illustrated in figure 1. The domain measures 40 mm in the r and z directions, and it contains a plate-plate geometry with a needle protrusion at the upper plate. To generate non-branching streamers with widely varying properties (such as radius and velocity), we use three different electrodes, with parameters described in table 1. These electrodes are rod-shaped with semi-spherical tips, with lengths L_{rod} of 2 mm, 4 mm and 6 mm, and radii R_{rod} of 0.2 mm, 0.4 mm and 0.6 mm, respectively. Except for a small region near the rod electrode, the axial electric field is approximately uniform and equal to the average electric field between two plate electrodes, which is here defined as the background electric field E_{bg}:

$$E_{bg} = V/d\,, \tag{4}$$

where $d = 40$ mm is the distance between two plate electrodes and V is the applied voltage.

For the electric potential, a Dirichlet boundary condition is applied on the upper plate and rod electrode (corresponding to the applied voltage). The lower plate is grounded, and a homogeneous Neumann boundary condition is applied on the outer axial boundary. For all plasma species densities, homogeneous Neumann boundary conditions are applied on all domain boundaries, including the rod electrode. Secondary electron emission from electrodes due to ions and photons is not included.

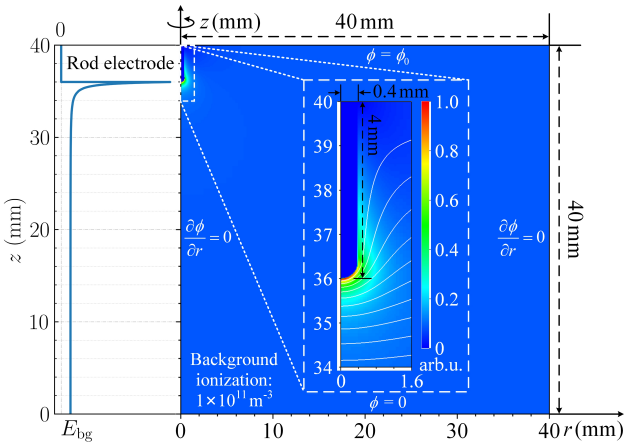

Figure 1: Schematic view of the 2D axisymmetric computational domain, measuring 40 mm × 40 mm. Right: the initial electric field without a streamer and the rod electrode geometry for $L_{rod} = 4$ mm and $R_{rod} = 0.4$ mm. Boundary conditions for the electric potential ϕ are also indicated. Left: the axial electric field. E_{bg} is the average electric field between two plate electrodes.

As an initial condition, homogeneous background ionization with a density of 10^{11} m^{-3} for both electrons and N_2^+ is included. All other ion densities are initially zero. The simulations are not sensitive to this background ionization density, because photoionization quickly becomes the dominant source of non-local free electrons after inception, see e.g. [50, 51].

For computational efficiency, the `Afivo-streamer` code includes adaptive mesh refinement. We use the same refinement criteria for the grid spacing Δx as [41], which lead to a minimal grid spacing of $\Delta x_{min} = 1.22\,\mu$m.

2.4. Voltage waveform

A single voltage pulse with a rise time of 1 ns is used, during which it increases linearly. The applied voltage is then constant until the streamer has reached a desired streamer length L_s (see table 1), after which the voltage is turned off linearly with a 1 ns fall time. The applied voltage V is varied to obtain different background electric fields E_{bg}, see table 1 and equation (4).

The streamer length L_s is defined as the distance between the rod electrode tip and the streamer position z_{head} at which the electric field has a maximum. We use such a length-dependent voltage waveform so that we can study the effect of L_s on energy efficiencies (due to more or less Joule heating in the channel, see section 5.1). Furthermore, it allows us to compare

Table 1: Summary of simulation parameters used for generating 60 positive streamers and 8 negative streamers.

Voltage polarity	Electrode length $L_{\rm rod}$	Electrode radius $R_{\rm rod}$	Steamer length $L_{\rm s}$	Range of background fields $E_{\rm bg}$	Number of cases
positive	2 mm	0.2 mm	18 mm	11.5–26 kV/cm	12
	4 mm	0.4 mm	10 mm	10–26 kV/cm	12
	4 mm	0.4 mm	18 mm	10–26 kV/cm	12
	4 mm	0.4 mm	26 mm	10–26 kV/cm	12
	6 mm	0.6 mm	18 mm	9–26 kV/cm	12
negative	6 mm	0.6 mm	18 mm	14–26 kV/cm	8

results at the same streamer lengths. All simulations are performed until $t = 500$ ns.

3. Example of streamer dynamics and chemistry

3.1. Streamer dynamics

We first present an example of a positive streamer in dry air. A background field $E_{\rm bg}$ of 14 kV/cm (half of the breakdown field of 28 kV/cm in air) was used, and the voltage was turned off after 19.8 ns. Furthermore, a rod electrode with length $L_{\rm rod} = 4$ mm and radius $R_{\rm rod} = 0.4$ mm and a desired streamer length $L_{\rm s} = 18$ mm were used. Figure 2 shows the time evolution of the electric field and electron density profiles for this example, together with its axial profiles.

The streamer initiates from the rod electrode tip, after which its velocity and radius increase almost linearly with time, from about 0.7×10^6 m/s to 1.4×10^6 m/s and from about 0.5 mm to 0.9 mm, respectively. The streamer radius is here defined as the electrodynamic radius at which the radial component of the electric field has a maximum.

The line conductivity σ^* at the streamer head also increases as the streamer grows, due to its increasing radius, from about 3×10^{-7} S·m to 3×10^{-6} S·m. Here σ^* is computed as

$$\sigma^*(z) = 2\pi e \int_0^{10\,\rm mm} r n_{\rm e} \mu_{\rm e} \, {\rm d}r \,, \tag{5}$$

where e is the elementary charge. In contrast, the electron density at the streamer head decreases slightly from about 6×10^{19} m^{-3} to 5×10^{19} m^{-3}, and the lowest internal on-axis electric field inside the streamer channel decreases from about 6 kV/cm to 4 kV/cm. However, the maximal electric field at the streamer head of about 120 kV/cm stays approximately constant during the voltage pulse.

After 19.8 ns the voltage is turned off and the streamer stops, but the simulation continues up to 500 ns. The streamer channel gradually loses its conductivity, with an about three orders of magnitude decrease in the electron density and line conductivity. The channel radius increases slightly from about 0.9 mm to 1.2 mm due to ion motion.

At 500 ns, the maximal electric field is about 2 kV/cm, and the lowest internal field is about 0.03 kV/cm. The total deposited energy $Q_{\rm total}$ at 500 ns is about 86 μJ, which is here computed as

$$Q_{\rm total} = \int_0^{T_{\rm total}} \int_\Omega j \cdot E \, {\rm d}\Omega {\rm d}t \,, \tag{6}$$

where $j = e n_{\rm e} \mu_{\rm e} E$ is the electron conduction current density, Ω the computational domain, and $T_{\rm total} = 500$ ns.

3.2. Plasma chemistry

We now look into the plasma chemistry of the streamer case mentioned above. We consider 56 chemically active species and 263 chemical reactions, as shown in table A2. A list of gross and net productions of all 56 species at $t = 500$ ns is given in table 2, in units of the number of molecules/atoms produced in some particular state. Here gross production means the total time and space integrated production of a specific species, without taking into account loss processes. For net production, loss processes are taken into account.

The time evolution of the gross and net production of 17 species is shown in figure 3, namely e (electrons), $N_2(J)$, $N_2(v)$, $O_2(J)$, $O_2(v)$, O_2(a), N(^{4}S), O(^{3}P), O_2^+, O_4^+, N_4^+, O_2^-, O_4^-, O_3, NO, NO_2 and N_2O. Note that the total vibrationally excited state $N_2(v)$ is the sum of each vibrationally excited state from $N_2(v_1)$ to $N_2(v_8)$, and the total vibrationally excited state $O_2(v)$ is the sum of each vibrationally excited state from $O_2(v_1)$ to $O_2(v_4)$.

Figure 3 shows that the gross and net production are the same for $N_2(J)$, $N_2(v)$, $O_2(J)$ and $O_2(v)$, because their loss reactions were not included, as discussed in Appendix A.1. For O_2(a), N(^{4}S), O(^{3}P), O_3, NO, NO_2 and N_2O, gross and net production are almost equal due to relatively slow loss processes. The

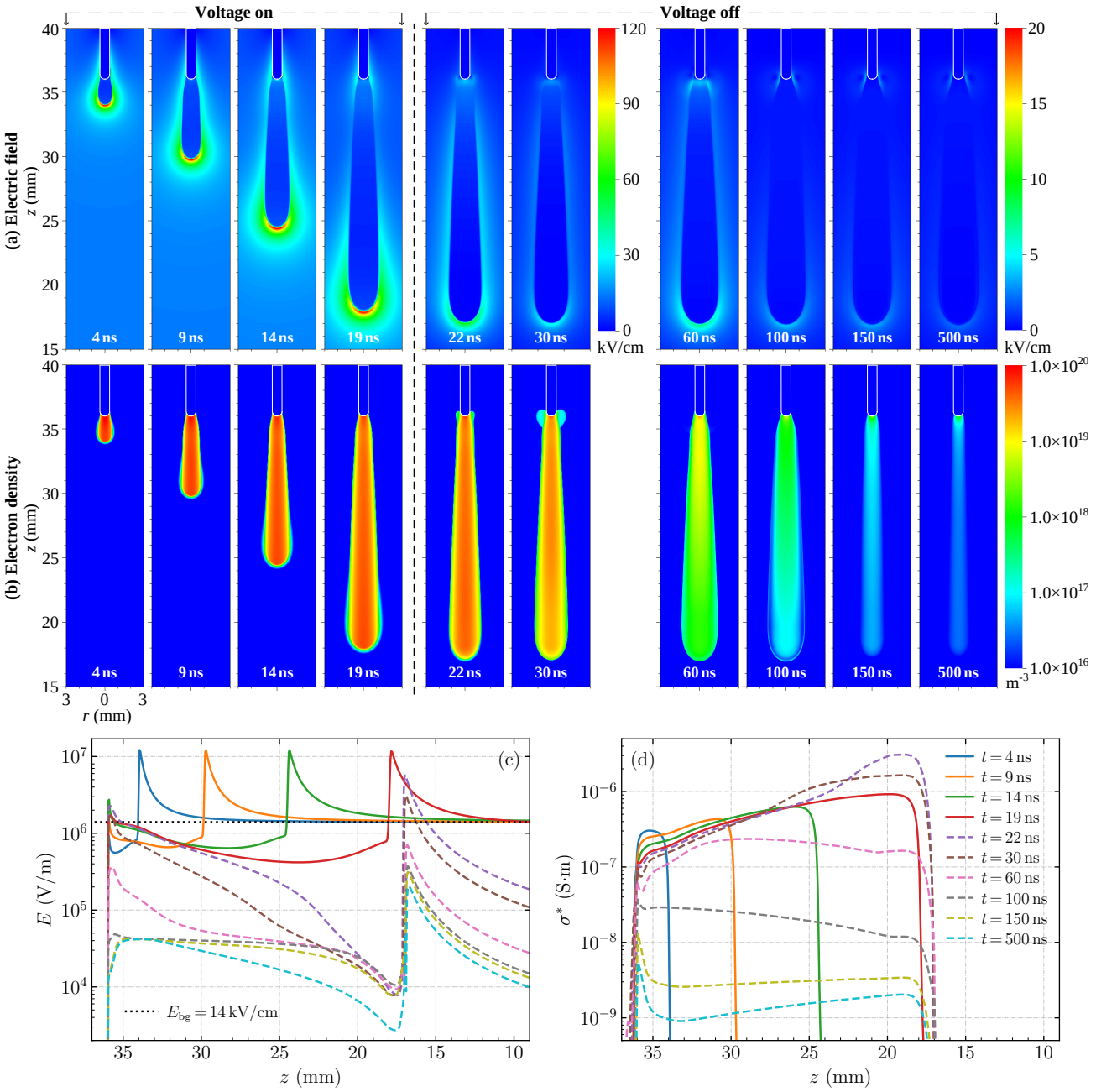

Figure 2: Time evolution of (a) the electric field E, (b) the electron density n_e, (c) the on-axis electric field E, and (d) the line conductivity σ^* for a positive streamer in $E_{bg} = 14\,\mathrm{kV/cm}$ with $L_{rod} = 4\,\mathrm{mm}$, $R_{rod} = 0.4\,\mathrm{mm}$ and $L_s = 18\,\mathrm{mm}$ in air. Note that profiles of E after 30 ns are shown on a different scale; for n_e the same scale is used at all times. Profiles of n_e are shown on a logarithmic scale. All panels in (a) and (b) are zoomed in into the region where $0 \leqslant r \leqslant 3\,\mathrm{mm}$ and $15 \leqslant z \leqslant 40\,\mathrm{mm}$. The solid and dashed lines in panels (c) and (d) correspond to the streamer before and after the voltage is turned off, respectively.

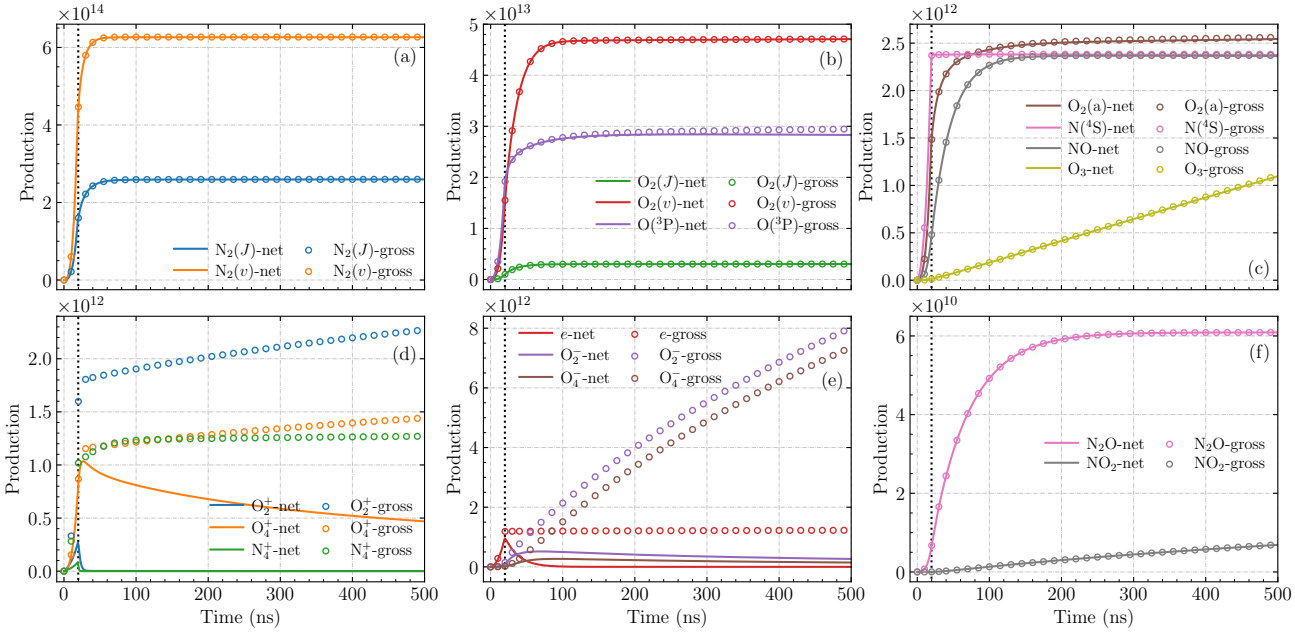

Figure 3: Time evolution of the gross and net productions of 17 species for the streamer corresponding to figure 2. The vertical dotted black lines correspond to the moment when the voltage is turned off, namely $t = 19.8$ ns.

gross and net production of $O(^3P)$ differ because $O(^3P)$ is primarily converted to O_3 by the reaction $O(^3P) + O_2 + M \rightarrow O_3 + M$. For charged species, net production is much lower than gross production since these species are rapidly converted to other species by attachment, detachment, ion conversion and recombination.

For most of the 17 species there is essentially no more production after 500 ns, with the exceptions being O_3, NO_2, O_2^+, O_4^+, N_4^+, O_2^- and O_4^-, which are produced relatively slowly. Note that there is continued gross production of both O_2^- and O_4^-, but no net production, due to the conversion between these species by reactions R69 and R81.

4. Parameter study of species production and energy efficiency

In this section, we simulate 60 positive streamers by varying the rod electrode length, rod electrode radius, desired streamer length and the background field as described in table 1. In figures 4 and 5, we compare the total net production and energy efficiencies for nine neutral species: $N_2(J)$, $N_2(v)$, $O_2(J)$, $O_2(v)$, O_2(a), $N(^4S)$, $O(^3P)$, NO and N_2O. To compare energy efficiencies, we use so-called G-values, which give the net number of atoms or molecules produced per 100 eV of deposited energy, at $t = 500$ ns. We find the highest G-values for $N_2(v)$, about 10^2, and the lowest for N_2O, about 10^{-2}.

Figure 4 shows that the total net production of the nine species increases with the background field and with the streamer length, as could be expected. A longer rod electrode leads to a wider and faster streamer and therefore also to more production.

Figure 5 shows that the G-values for $N_2(v)$, O_2(a), $N(^4S)$, $O(^3P)$, NO and N_2O vary by at most 30% to 60%. Larger variation of about 70% to 120% can be observed for $N_2(J)$, $O_2(J)$ and $O_2(v)$. The dependence of the G-value on the background field for nine species can be grouped into three categories. For $N(^4S)$, $O(^3P)$, NO and N_2O, G-values first slightly decrease and then increase with the background field, whereas for $N_2(J)$, $N_2(v)$, $O_2(J)$ and $O_2(v)$ G-values monotonically decrease with the background field. For O_2(a), G-values first decrease and then slightly increase with the background field. These different dependencies can be explained by considering the activation energies for the reactions producing these species.

The key reactions producing $N(^4S)$, $O(^3P)$, NO and N_2O have high activation energies ranging from 6 eV to 13 eV, so they are primarily produced in the high electric field near the streamer head, as illustrated in figure 6 for $N(^4S)$. Specifically, $N(^4S)$ and NO are mostly produced by an electron dissociation reaction, namely $e + N_2 \rightarrow e + N(^4S) + N(^2D)$, and the N_2O production depends on electronic excitation reactions producing N_2(A) and N_2(B). $O(^3P)$ production is determined by electron dissociation reactions of nitrogen and oxygen molecules, as well as electronic excitation reactions of nitrogen, e.g., N_2(B).

Figure 7(a) shows the relation between the average

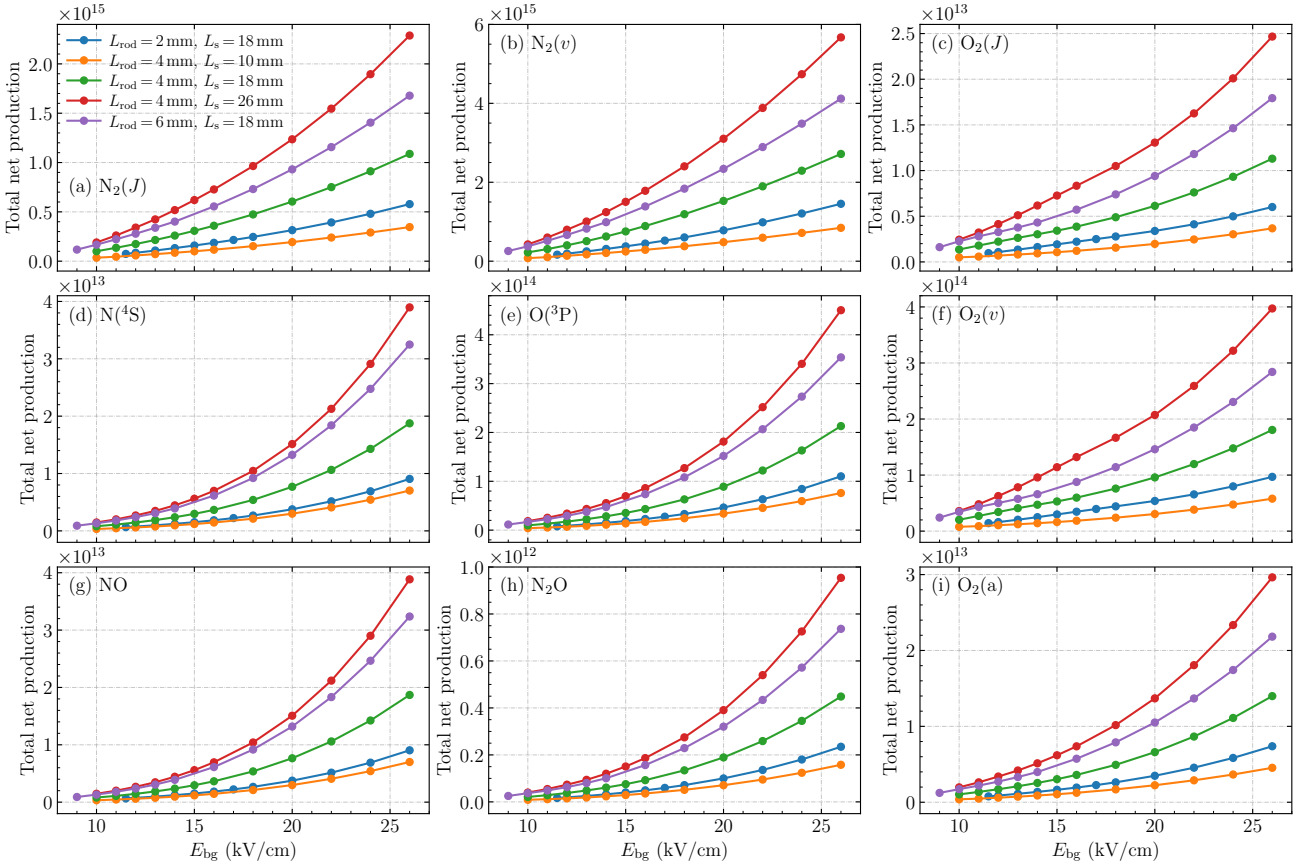

Figure 4: The total net production at 500 ns of nine species versus the background field E_{bg}. Results are shown for 60 positive streamers in different background fields with different electrode geometries ($L_{rod} = 2, 4, 6$ mm, $R_{rod} = 0.2, 0.4, 0.6$ mm) and different streamer lengths ($L_s = 10, 18, 26$ mm), see table 1.

maximal electric field $\overline{E}_{max}$ and the background field E_{bg} for the 60 streamer cases. Here $\overline{E}_{max}$ is an average over the time when the voltage is at its peak. Note that $\overline{E}_{max}$ depends non-monotonically on the background field: it increases for both the highest and lowest considered background fields, as was also observed in [52]. This explains the similarly non-monotonic dependence of the G-values for $N(^4S)$, $O(^3P)$, NO and N_2O shown in figure 5, since there is an approximately linear relation between $\overline{E}_{max}$ and these G-values, as illustrated in figure 7(b). We remark that it was difficult to avoid streamer branching in simulations in low background fields, so we could not fully explore the increase in G-values for low background fields.

In contrast, the electron-molecule reactions producing $N_2(J)$, $N_2(v)$, $O_2(J)$ and $O_2(v)$ have lower activation energies, below about 2 eV. These reactions therefore primarily take place inside the streamer channel, where the electron density is high, as illustrated in figure 6 for $N_2(J)$. Specifically, $N_2(J)$ and $O_2(J)$ are produced by rotational excitations of nitrogen and oxygen molecules, and $N_2(v)$ and $O_2(v)$ by vibrational excitations. Figure 4 shows that the production of $N_2(J)$, $N_2(v)$, $O_2(J)$ and $O_2(v)$ increases for higher background fields, but that the production of $N(^4S)$, $O(^3P)$, NO and N_2O increases even more rapidly, so that G-values for $N_2(J)$, $N_2(v)$, $O_2(J)$ and $O_2(v)$ decrease.

The production of O_2(a) falls somewhat between these two regimes, because it can be produced by reactions with different activation energies. There is a direct electronic excitation reaction generating O_2(a) with an activation energy of 0.977 eV, but O_2(a) is also produced indirectly from N_2(A) and N_2(B), which correspond to higher activation energies, ranging from 6.17 eV to 8.16 eV. Due to these different mechanisms, O_2(a) is both produced inside the streamer channel and in the high electric field near the streamer head, as shown in figure 6.

5. Other results and discussion

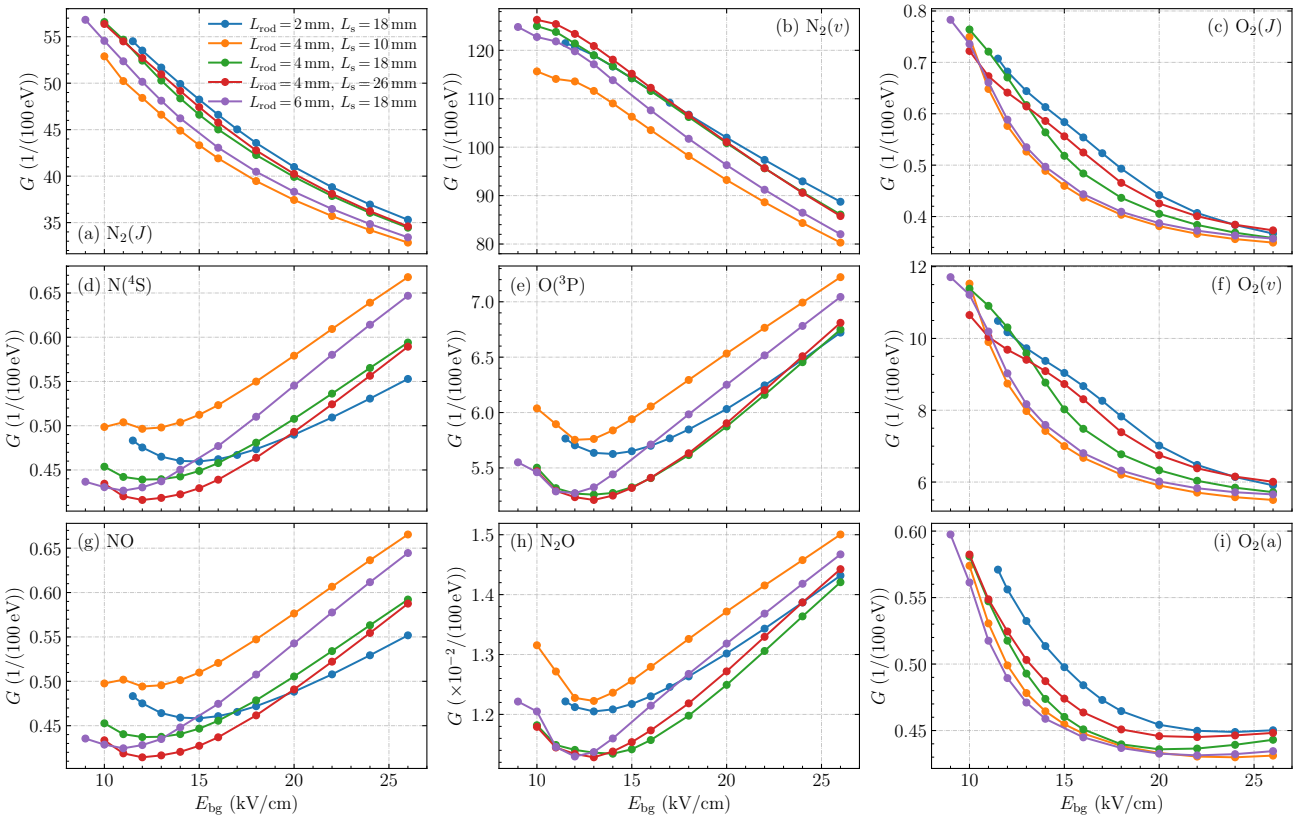

Figure 5: G-values for the production of nine species versus the background field E_{bg} for the 60 streamers corresponding to figure 4.

5.1. Comparison with Naidis' estimate

In [33], Naidis proposed that "the maximum G-values are governed by only one parameter – the reduced electric field in the streamer head Y_h, and that their dependence on Y_h in the typical range of propagating streamers is not strong, when both generation of active species and energy input occur mainly in the streamer head region." The paper contains an analytic approximation for G-values, that we for clarity rewrite as:

$$G_j = \frac{2n_j}{eE_{max}^2} \int_{E_{ch}}^{E_{max}} \frac{K_j}{\mu_e E}\, dE\,, \tag{7}$$

where E_{max} is the maximal electric field at the streamer head, E_{ch} the electric field in the streamer channel, n_j the number density of molecules producing species j, K_j the field-dependent rate coefficient of electron-molecule reaction producing species j, and E is the electric field. The integral is not sensitive to the particular value used for E_{ch}, since it is meant to be used for species mainly produced in high electric fields, so we for simplicity use $E_{ch} = 0$ below. Several approximations are made to derive equation (7): the streamer is assumed to be uniformly translating, the streamer head is locally assumed to be flat, so that one-dimensional integration can be performed, and Joule heating in the streamer channel is not taken into account.

As discussed in [33], it can be important to take Joule heating in the streamer channel into account. We obtain this correction by measuring the deposited power in the streamer channel and in the streamer head region, as shown in figure 8. The streamer head region was defined as the region where $E \geqslant 28\,kV/cm$. There is still some Joule heating in the streamer channel after the voltage is turned off, which corresponds to currents that screen the electric field generated by the remaining space charge. The fraction of power deposited in the channel increases with time. However, even for short primary streamers, on time scales well below 10 ns, Joule heating in the streamer channel can still be important.

A correction factor Q_{head}/Q_{total}, i.e., the fraction of total energy deposited in the streamer head region, is computed by integrating the deposited power over time. As shown in figure 8(d), this factor lies between 0.35 and 0.5 for the 60 positive cases considered in this paper. Note that Q_{head}/Q_{total} first decreases and then increases with the background field, similar to $\overline{E}_{max}$ shown in figure 7(a).

Table 2: The gross and net productions of all 56 species for the streamer corresponding to figure 2 at $t = 500\,\text{ns}$. Production below 10^3 has been replaced by ~ 0.

Species	Gross production	Net production
$N_2(J)$	2.60×10^{14}	2.60×10^{14}
$N_2(v_1)$	3.50×10^{14}	3.50×10^{14}
$N_2(v_2)$	1.39×10^{14}	1.39×10^{14}
$N_2(v_3)$	7.91×10^{13}	7.91×10^{13}
$N_2(v_4)$	2.86×10^{13}	2.86×10^{13}
$N_2(v_5)$	1.78×10^{13}	1.78×10^{13}
$N_2(v_6)$	7.92×10^{12}	7.92×10^{12}
$N_2(v_7)$	2.83×10^{12}	2.83×10^{12}
$N_2(v_8)$	9.96×10^{11}	9.96×10^{11}
N_2(A)	2.96×10^{12}	3.03×10^{8}
N_2(B)	5.44×10^{12}	~ 0
N_2(a)	2.66×10^{12}	~ 0
N_2(C)	2.48×10^{12}	~ 0
N_2(E)	1.69×10^{11}	~ 0
$O_2(J)$	3.03×10^{12}	3.03×10^{12}
$O_2(v_1)$	3.41×10^{13}	3.41×10^{13}
$O_2(v_2)$	9.58×10^{12}	9.58×10^{12}
$O_2(v_3)$	2.61×10^{12}	2.61×10^{12}
$O_2(v_4)$	8.04×10^{11}	8.04×10^{11}
O_2(a)	2.56×10^{12}	2.54×10^{12}
O_2(b)	3.15×10^{12}	3.09×10^{12}
O_2(A)	1.09×10^{12}	1.71×10^{11}
$N(^4S)$	2.38×10^{12}	2.38×10^{12}
$N(^2D)$	2.38×10^{12}	1.66×10^{5}
$N(^2P)$	4.57×10^{8}	2.91×10^{6}
$O(^3P)$	2.95×10^{13}	2.83×10^{13}
$O(^1D)$	5.48×10^{12}	7.08×10^{8}
$O(^1S)$	2.16×10^{12}	1.16×10^{12}
O_3	1.10×10^{12}	1.10×10^{12}
NO	2.37×10^{12}	2.36×10^{12}
NO_2	6.94×10^{9}	6.89×10^{9}
NO_3	5.30×10^{6}	5.18×10^{6}
N_2O	6.09×10^{10}	6.09×10^{10}
N_2O_3	~ 0	~ 0
N_2O_4	~ 0	~ 0
N_2O_5	6.53×10^{3}	6.53×10^{3}
e	1.23×10^{12}	7.17×10^{8}
O^-	8.91×10^{10}	5.60×10^{8}
O_2^-	8.02×10^{12}	2.66×10^{11}
O_3^-	9.70×10^{10}	5.73×10^{10}
O_4^-	7.36×10^{12}	1.46×10^{11}
NO^-	1.60×10^{7}	1.60×10^{7}
NO_2^-	2.50×10^{7}	2.50×10^{7}
NO_3^-	1.22×10^{9}	1.22×10^{9}
N_2O^-	5.79×10^{4}	5.79×10^{4}
N^+	4.34×10^{5}	4.34×10^{5}
N_2^+	8.96×10^{11}	2.23×10^{6}
N_3^+	1.49×10^{6}	1.49×10^{6}
N_4^+	1.27×10^{12}	~ 0
O^+	4.70×10^{7}	4.70×10^{7}
O_2^+	2.27×10^{12}	1.11×10^{9}
O_4^+	1.44×10^{12}	4.69×10^{11}
NO^+	1.62×10^{9}	1.62×10^{9}
NO_2^+	7.72×10^{6}	7.72×10^{6}
N_2O^+	~ 0	~ 0
$N_2O_2^+$	1.20×10^{12}	2.91×10^{7}

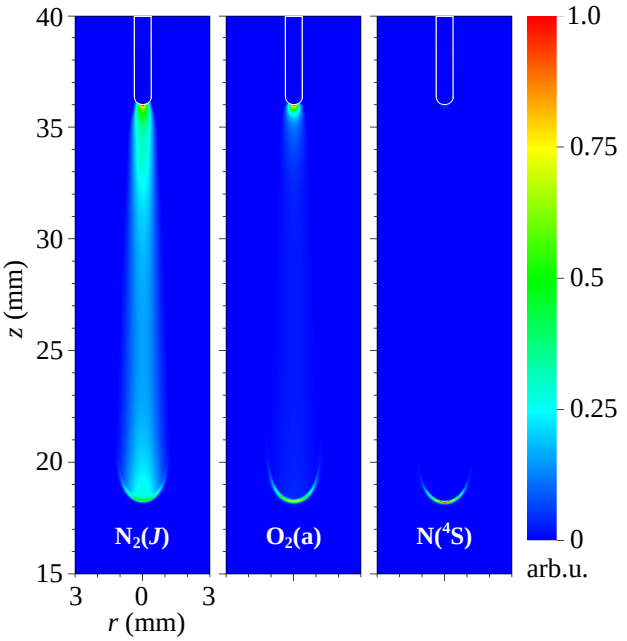

Figure 6: The instantaneous production of $N_2(J)$, O_2(a) and $N(^4S)$ at $t = 18.8\,\text{ns}$ for the streamer corresponding to figure 2. $N_2(J)$ is mostly produced in the channel, $N(^4S)$ mostly in the head and O_2(a) is produced in both. Profiles are shown using arbitrary units.

In figure 7(b), we compare equation (7) corrected with the factors $Q_{\text{head}}/Q_{\text{total}}$ from figure 8(d) against simulation results, for the production of $N(^4S)$. For this comparison, we use $E_{\max} = \overline{E}_{\max}$ and $E_{\text{ch}} = 0$ in equation (7). The agreement is then surprisingly good, with deviations of up to about 25%. We remark that the variation of equation (7) is about 20% in the considered maximal field range, which is smaller than the variation in the correction factor from figure 8(d), which is about 40%.

5.2. Comparison with negative streamers

We now compare the species production and G-values for $N(^4S)$, $O(^3P)$ and NO between positive and negative streamers in different background fields, as described in table 1. A rod electrode with length $L_{\text{rod}} = 6\,\text{mm}$ and radius $R_{\text{rod}} = 0.6\,\text{mm}$ and a desired streamer length $L_{\text{s}} = 18\,\text{mm}$ were used. Positive and negative streamers were obtained by changing the applied voltage polarity, while keeping all other simulation conditions the same.

In the background fields considered here, negative streamers have lower maximal electric fields than positive ones, as shown in figure 9 and also obtained previously [53, 54]. Figure 10 shows that total net production and G-values for $N(^4S)$, $O(^3P)$ and NO are

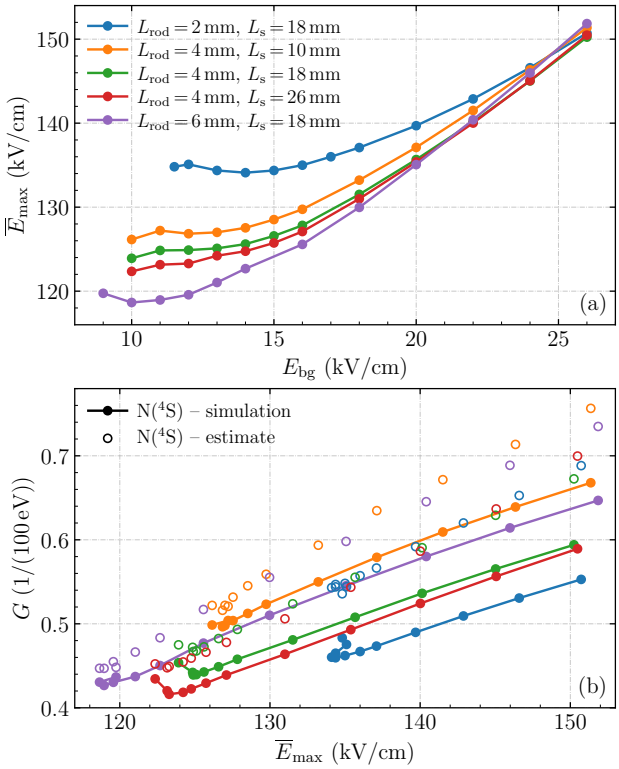

Figure 7: (a) The average maximal electric field $\overline{E}_{max}$ versus the background field E_{bg} for the 60 streamers corresponding to figure 4. (b) The simulated and estimated G-values for N(^{4}S) versus $\overline{E}_{max}$ corresponding to panel (a). The symbols correspond to the 60 simulated cases, by taking an average over the time when the voltage is at its peak for $\overline{E}_{max}$, by taking simulated G-values at $t = 500\,ns$ and by taking estimated G-values from equation (7) corrected with the factor Q_{head}/Q_{total} from figure 8(d).

also lower for negative streamers, with the G-values for N(^{4}S) and NO being up to 60% lower compared to positive streamers.

Furthermore, we again compare our results with Naidis' estimate, as discussed in section 5.1. Figure 9(d) shows that the correction factor Q_{head}/Q_{total} is smaller for negative streamers, indicating that more energy is deposited in the negative streamer channel. As shown in figure 9(e), the simulated G-values for N(^{4}S) agree well with estimated G-values for both positive and negative streamers. For both polarities the same approximately linear relationship between G-values and $\overline{E}_{max}$ can be observed.

We remark that in [55], the authors experimentally measured the energy efficiency of oxygen radical production in primary and secondary streamers for both voltage polarities. In contrast to our results, they found a higher energy efficiency for negative streamers,

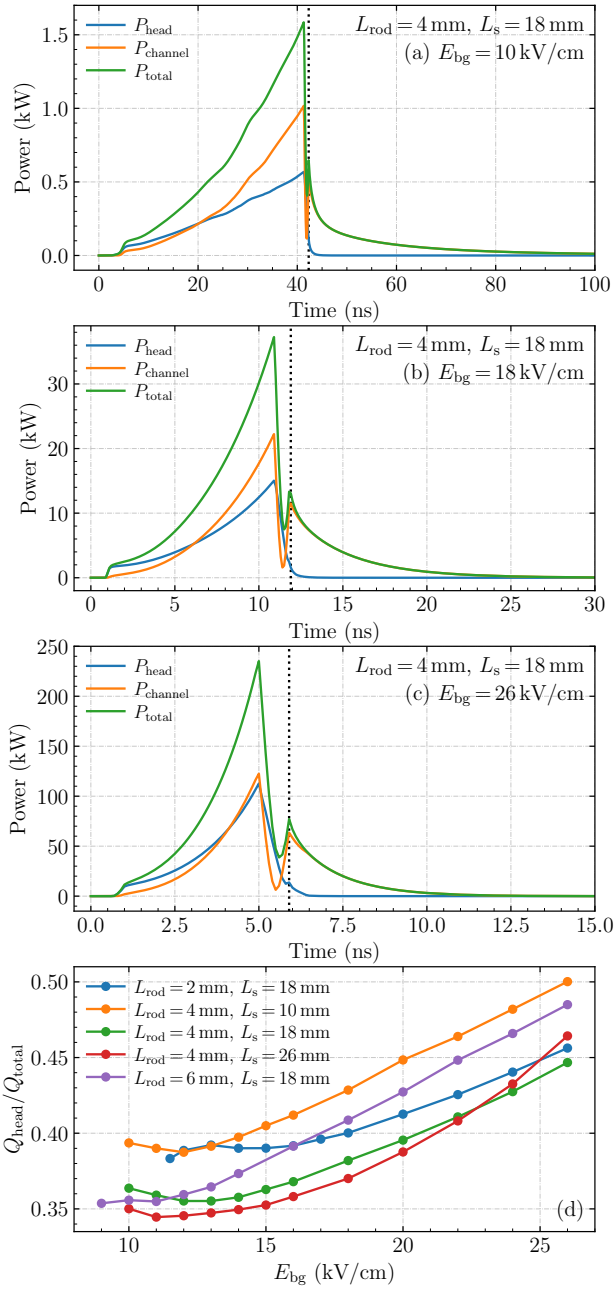

Figure 8: Time evolution of total deposited power P_{total}, power in the streamer head region P_{head} and in the streamer channel $P_{channel}$ for three positive streamers in E_{bg} of (a) 10 kV/cm, (b) 18 kV/cm and (c) 26 kV/cm with $L_{rod} = 4\,mm$, $R_{rod} = 0.4\,mm$ and $L_s = 18\,mm$. The vertical dotted black lines correspond to the moment when the applied voltage has dropped to zero (after a 1 ns fall time). The streamer head region is defined as the region where $E \geqslant 28\,kV/cm$. (d) The fraction of energy deposited in the streamer head region Q_{head}/Q_{total} versus the background field E_{bg} for the 60 streamers corresponding to figure 4.

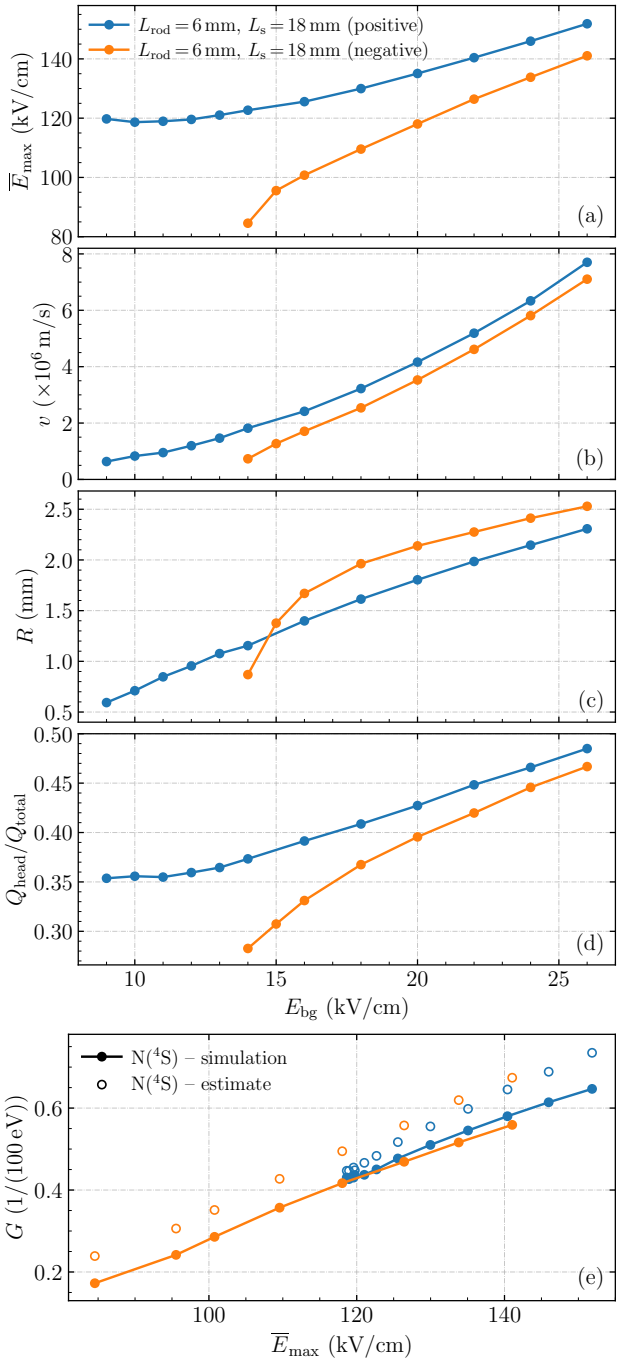

Figure 9: Comparison of positive and negative streamers, with parameters described in table 1. (a) Time-averaged maximal electric field $\overline{E}_{max}$, (b) velocity v, (c) radius R and (d) fraction of energy deposited in the streamer head region Q_{head}/Q_{total}, all versus the background field E_{bg}. The velocity and radius are given at the moment each streamer reached $L_s = 18$ mm. (e) The simulated and estimated G-values for N(^{4}S) versus $\overline{E}_{max}$ corresponding to panel (a). The estimated G-values from equation (7) were corrected with the factor Q_{head}/Q_{total} from panel (d).

but they noted that this efficiency could not accurately be measured for negative streamers due to a larger mismatch of the source impedance.

5.3. Qualitative comparison with experimental data for O_3

O_3 is produced relatively slowly, on time scales significantly longer than the 500 ns considered here, as shown in figure 3. In experiments, O(^{3}P) production is usually inferred from the measured O_3 production since most (e.g. 85%) of O(^{3}P) is converted to O_3 by $O(^3P) + O_2 + M \rightarrow O_3 + M$. In our simulations we can therefore estimate G-values for O_3 based on the O(^{3}P) production, which gives G-values of about 5–7, see figure 5(e).

We can compare these simulated G-values to experimentally obtained ones. However, there are many differences between our simulations and typical experiments, for example in the pulse repetition rate, pulse width, humidity, streamer branching and electrode geometry. The comparison below is therefore purely qualitative, to check whether the simulated G-values are roughly comparable to those in experiments.

In [56], the authors found G-values for O_3 production in $O_2(20\%)/N_2$ of about 4–6, using a 1 Hz pulse repetition rate in a point-plane gap. Furthermore, it was observed that the energy efficiency of O_3 production was enhanced by reducing the pulse width, and that production was more efficient in primary streamers than in secondary streamers. In [57], G-values for O_3 in air of about 2.5–3.4 were found, in a large scale wire-plate reactor with a relative humidity ranging from 35% to 42% and pulse repetition rates of 10–400 Hz. It was observed that short pulses increased energy efficiencies of O_3 production. In [58], a higher G-value of about 13 was measured for O_3 in dry air at a pulse repetition rate of 30 Hz in a wire-to-cylinder electrode reactor, using a short voltage pulse of 5 ns. In [55], the authors proposed that primary streamers were more efficient than secondary streamers for O_3 production, and G-values of about 10–16 were found for primary positive streamers in air in a wire-plate geometry with pulse repetition rates of 50–100 Hz, and relative humidity of 13–18%.

In conclusion, the simulated G-values agree within a factor of two to three with the listed experimental data, which seems reasonable given the different conditions at which the experiments were performed.

6. Conclusions and outlook

We have studied how the plasma chemistry of streamer discharges in dry air varies with streamer properties. Simulations were performed at 300 K and 1 bar in a 40 mm plane-plane gap with a needle protrusion, using

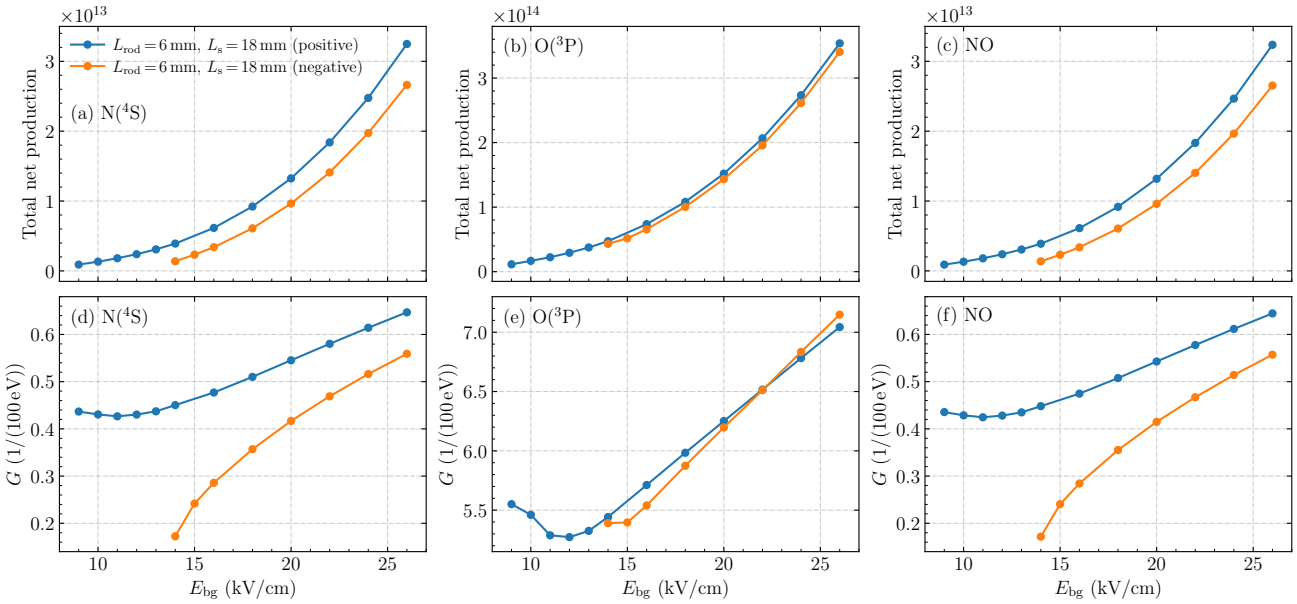

Figure 10: The total net production and G-values for N(^{4}S), O(^{3}P) and NO versus the background field E_{bg} for both positive and negative streamers with $L_{rod} = 6\,\text{mm}$, $R_{rod} = 0.6\,\text{mm}$ and $L_s = 18\,\text{mm}$.

a 2D axisymmetric fluid model. Sixty different positive streamers were obtained by varying the electrode geometry, the applied voltage and the duration of the voltage pulse. The obtained streamers had diameters ranging from about 0.5 mm to 3.5 mm, velocities ranging from about 0.3×10^6 m/s to 5.7×10^6 m/s and maximal electric fields ranging from about 120 kV/cm to 150 kV/cm.

For species with a relatively high activation energy, such as N(^{4}S), O(^{3}P), NO and N_2O, G-values were found to vary by about 30% to 60% between the 60 positive cases. The most important factors behind this variation were differences in the fraction of energy deposited in the streamer head region and variation in the maximal electric field at the streamer head. When accounting for both factors, good agreement was obtained with an analytic estimate for G-values proposed by Naidis [33]. For comparison, eight negative streamers were also simulated. They were found to be less energy efficient for the production of N(^{4}S), O(^{3}P) and NO, mainly due to a lower maximal electric field and because more energy was deposited in the streamer channel.

Our results suggest two main ways to increase the energy efficiency with which species with a high activation energy are produced. First, Joule heating losses in the streamer channel can be reduced, and second, the maximal reduced electric field at the streamer head can be increased. Short voltage pulses with a high applied voltage can contribute to both factors.

Outlook. In future work, it would be interesting to study the effect of repetitive pulses, as well as gas heating and humidity effects, and to directly compare with experimental data. Another question is whether electric fields at streamer heads can be increased by reducing photoionization (for example through the addition of CO_2 [59]), as this leads to more frequent branching and narrower channels. Furthermore, it would be interesting to study whether "minimal streamers" in low background fields can achieve a high energy efficiency for species production, due to their high maximal electric field [52].

Finally, we think testing and improving the validity of the reaction set is of high importance. This requires careful comparisons against experiments, in which techniques such as optical emission spectroscopy, mass spectrometry or laser-based diagnostics could be used to measure concentrations of neutral, excited and ionized species, as reviewed in e.g. [1, 60].

Acknowledgments

B.G. was funded by the China Scholarship Council (CSC) (Grant No. 201906280436). We thank Dr. Atsushi Komuro from the University of Tokyo for sharing chemical reactions, and we thank Prof. Dr. Ute Ebert, Dr. Bastiaan Braams and Mr. Hemaditya Malla at CWI for their suggestions for improvements.

Data availability statement

The data that support the findings of this study are openly available at the following URL/DOI: `https:`

//doi.org/10.5281/zenodo.7093075. Any feedback on the reaction set is welcome.

Appendix A. The reaction set

Table A1 lists the excited states of N_2 and O_2 included in the model, as well as their activation energies. The 263 chemical reactions used in the simulations are given in table A2, with their rate coefficients and references. This reaction set contains different processes: rotational excitation, vibrational excitation, electron excitation, electron dissociation, electron impact ionization, electron attachment, electron detachment, negative ion conversion, positive ion conversion, electron-ion recombination, ion-ion recombination and neutral species conversion.

Appendix A.1. Comments on the reaction set

The reaction set was constructed for streamer simulations in dry air at 300 K and 1 bar, considering relatively short time scales (up to several microseconds). Below we give some comments on the reaction set.

- Some of the reaction rate coefficients have to be adjusted when going to different pressures.
- Only reactions between electrons and ground-state molecules are taken into account.
- No reactions are included to describe the evolution of vibrationally excited states. Such reactions are for example given in [61].
- We have not tried to consistently include loss reactions (or reverse reactions) for all species.
- There are in particular no loss reactions for $N_2(J)$, $N_2(v)$, $O_2(J)$ and $O_2(v)$. When considering secondary streamers, $N_2(v)$ dissociation by electrons can play a role in nitrogen radical formation [42].
- High vibrationally excited states $N_2(v > 8)$ and $O_2(v > 4)$ are ignored. Such states of N_2 can for example contribute to nitrogen radical formation [33].
- We have not separated $N_2(A)$ into $N_2(A_1)$ and $N_2(A_2)$, as was done in e.g. [22, 29].
- Reactions R36 and R201 are actually three-body reactions. These reactions are included as two-body processes because the intermediate states have long lifetimes [19].
- The rate coefficient for reaction R73 is given as $k < 1 \times 10^{-12}\,\mathrm{cm^3\,s^{-1}}$ in [19]. The upper limit ($k = 1 \times 10^{-12}$) is used here.
- The three-body reactions R89, R97 and R104 include M (any molecule) as a third body. Note that in [19] only specific reactions with N_2 or O_2 are given. However, based on [21, 62] we think using a generic third body is better. The rate coefficients for reactions R89 and R104 are taken from [21], and for reaction R97 taken from [19].
- For reaction R121 we assume the 'N' from [19] refers to $N(^4S)$. However, more recent work [25] suggests that this reaction produces $N(^2D)$.
- The two-body dissociative reaction of e with O_2^+ can produce $O(^3P)$ and $O(^1D)$ through different channels. Based on table 30 of [25], the production of $O(^3P)$ and $O(^1D)$ is approximately the same. For simplicity, we therefore use only one channel producing $O(^3P) + O(^1D)$ in reaction R125.
- For reactions R157, R159 and R161 from [26], there might be an "overlap" with reactions R156, R158 and R160 [19].
- Regarding reactions R163 and R164: a total reaction rate coefficient for producing O_2(a) or O_2(b) is given in [19]. From this total rate coefficient we subtracted the rate coefficient for reaction R164 [27] to obtain reaction R163.
- Reactions R196, R234 and R235 from [19] can produce excited states, but due to a lack of data we assume only molecules in the ground state are produced.

Appendix A.2. Example of an invalid reaction rate coefficient

When preparing the reaction set, we also encountered reactions that we later had to exclude. One such example is the reaction $O_4^+ + O^- \rightarrow O_2 + O_3$ from [23] (2002), with a rate coefficient

$$k = 7.80 \times 10^{-6}\,\mathrm{cm^3\,s^{-1}},$$

citing earlier work [63] (1991). In [63], the rate coefficient is actually given as

$$k = 4.0{\times}10^{-7}(300/T)^{0.5}{+}3.0{\times}10^{-25}(300/T)^{2.5} M\,\mathrm{cm^3\,s^{-1}},$$

where T is the gas temperature in Kelvin and M is the neutral gas number density, citing [64] (1975). In [64], the same rate coefficient can be found (but in a different notation), referring to the third revision of the Defense Nuclear Agency (DNA) Reaction Rate Handbook [65] (1973). We could not obtain the third revision, but in the seventh revision of the DNA handbook, a general recombination reaction of the form

$$X^+ + Y^- \rightarrow \text{products},$$

is given, with a rate coefficient

$$k = 1.0 \times 10^{-7}(300/T)^{0.5},$$

with an uncertainty interval of $(1.0 - 0.6) \times 10^{-7}$ to $(1.0 + 4.0) \times 10^{-7}$. This last rate coefficient is almost

Table A1: Excited states of N_2 and O_2 with activation energies and the corresponding effective states used in the model. The table is partially based on the one in [29].

Excited state	Activation energy ϵ_e (eV)	Effective state
N_2(rot)	0.02	$N_2(J)$
$N_2(X,\, v=1)$	0.29	$N_2(v_1)$
$N_2(X,\, v=2)$	0.59	$N_2(v_2)$
$N_2(X,\, v=3)$	0.88	$N_2(v_3)$
$N_2(X,\, v=4)$	1.17	$N_2(v_4)$
$N_2(X,\, v=5)$	1.47	$N_2(v_5)$
$N_2(X,\, v=6)$	1.76	$N_2(v_6)$
$N_2(X,\, v=7)$	2.06	$N_2(v_7)$
$N_2(X,\, v=8)$	2.35	$N_2(v_8)$
$N_2(A^3\Sigma_u^+,\, v=0...4)$	6.17	N_2(A)
$N_2(A^3\Sigma_u^+,\, v=5...9)$	7.00	N_2(A)
$N_2(B^3\Pi_g)$	7.35	N_2(B)
$N_2(W^3\Delta_u)$	7.36	N_2(B)
$N_2(A^3\Sigma_u^+,\, v>10)$	7.80	N_2(B)
$N_2(B'^3\Sigma_u^-)$	8.16	N_2(B)
$N_2(a'^1\Sigma_u^-)$	8.40	N_2(a)
$N_2(a^1\Pi_g)$	8.55	N_2(a)
$N_2(w^1\Delta_u)$	8.89	N_2(a)
$N_2(C^3\Pi_u)$	11.03	N_2(C)
$N_2(E^3\Sigma_g^+)$	11.87	N_2(E)
$N_2(a''^1\Sigma_g^+)$	12.25	N_2(E)
O_2(rot)	0.02	$O_2(J)$
$O_2(X,\, v=1)$	0.19	$O_2(v_1)$
$O_2(X,\, v=2)$	0.38	$O_2(v_2)$
$O_2(X,\, v=3)$	0.57	$O_2(v_3)$
$O_2(X,\, v=4)$	0.75	$O_2(v_4)$
$O_2(a^1\Delta_g)$	0.977	O_2(a)
$O_2(b^1\Sigma_g^+)$	1.627	O_2(b)
$O_2(c^1\Sigma_u^-)$	4.05	O_2(A)
$O_2(A'^3\Delta_u)$	4.26	O_2(A)
$O_2(A^3\Sigma_u^+)$	4.34	O_2(A)

two orders of magnitude lower than the one from [23], but it is consistent with [19] and most other literature. We can therefore conclude that the coefficients given in [23,63,64] for this recombination reaction (and other similar ones) are likely wrong.

References

[1] Sander Nijdam, Jannis Teunissen, and Ute Ebert. The physics of streamer discharge phenomena. *Plasma Sources Science and Technology*, 29(10):103001, November 2020.

[2] Douyan Wang and Takao Namihira. Nanosecond pulsed streamer discharges: II. Physics, discharge characterization and plasma processing. *Plasma Sources Science and Technology*, 29(2):023001, February 2020.

[3] Peter J Bruggeman, Felipe Iza, and Ronny Brandenburg. Foundations of atmospheric pressure non-equilibrium plasmas. *Plasma Sources Science and Technology*, 26(12):123002, November 2017.

[4] Hyun-Ha Kim. Nonthermal Plasma Processing for Air-Pollution Control: A Historical Review, Current Issues, and Future Prospects. *Plasma Processes and Polymers*, 1(2):91–110, September 2004.

[5] G.J.J. Winands, K. Yan, A.J.M. Pemen, S.A. Nair, Z. Liu, and E.J.M. Van Heesch. An Industrial Streamer Corona Plasma System for Gas Cleaning. *IEEE Transactions on Plasma Science*, 34(5):2426–2433, October 2006.

[6] Xianjun He, Yuxuan Zeng, Jialin Chen, Fushan Wang, Yunqing Fu, Fada Feng, and Haibao Huang. Role of O_3 in the removal of HCHO using a DC streamer plasma. *Journal of Physics D: Applied Physics*, 52(46):465203, November 2019.

[7] Nan Jiang, Xiaoqi Kong, Xiaoling Lu, Bangfa Peng, Zhengyan Liu, Jie Li, Kefeng Shang, Na Lu, and Yan Wu. Promoting streamer propagation, active species generation and trichloroethylene degradation using a three-electrode nanosecond pulsed sliding DBD nanosecond plasma. *Journal of Cleaner Production*, 332:129998, January 2022.

[8] Ravil H. Amirov, Jae O. Chae, Yuriy N. Dessiaterik, Elena A. Filimonova, and Mark B. Zhelezniak. Removal of NO_x and SO_2 from Air Excited by Streamer Corona: Experimental Results and Modeling. *Japanese Journal of Applied Physics*, 37(Part 1, No. 6A):3521–3529, June 1998.

[9] Hisanao Hazama, Masanori Fujiwara, and Mitsumori Tanimoto. Removal processes of nitric oxide along positive streamers observed by laser-induced fluorescence imaging spectroscopy. *Chemical Physics Letters*, 323(5-6):542–548, June 2000.

[10] T. Kuroki, M. Takahashi, M. Okubo, and T. Yamamoto. Single-stage plasma-chemical process for particulates, NO_x, and SO_x simultaneous removal. *IEEE Transactions on Industry Applications*, 38(5):1204–1209, September 2002.

[11] Mayank Sahni and Bruce R. Locke. Degradation of chemical warfare agent simulants using gas–liquid pulsed streamer discharges. *Journal of Hazardous Materials*, 137(2):1025–1034, September 2006.

[12] Ravindra P. Joshi and Selma Mededovic Thagard. Streamer-Like Electrical Discharges in Water: Part II. Environmental Applications. *Plasma Chemistry and Plasma Processing*, 33(1):17–49, February 2013.

[13] L. Bárdos and H. Baránková. Cold atmospheric plasma: Sources, processes, and applications. *Thin Solid Films*, 518(23):6705–6713, September 2010.

[14] O. Polonskyi, T. Hartig, J. R. Uzarski, and M. J. Gordon. Precise localization of DBD plasma streamers using topographically patterned insulators for maskless structural and chemical modification of surfaces. *Applied Physics Letters*, 119(21):211601, November 2021.

[15] Gregory Fridman, Gary Friedman, Alexander Gutsol, Anatoly B. Shekhter, Victor N. Vasilets, and Alexander Fridman. Applied Plasma Medicine. *Plasma Processes and Polymers*, 5(6):503–533, August 2008.

[16] Thomas von Woedtke, Steffen Emmert, Hans-Robert Metelmann, Stefan Rupf, and Klaus-Dieter Weltmann. Perspectives on cold atmospheric plasma (CAP) applications in medicine. *Physics of Plasmas*, 27(7):070601, July 2020.

[17] S M Starikovskaia. Plasma-assisted ignition and combustion: Nanosecond discharges and development of kinetic mechanisms. *Journal of Physics D: Applied Physics*, 47(35):353001, September 2014.

[18] N A Popov. Kinetics of plasma-assisted combustion: Effect of non-equilibrium excitation on the ignition and oxidation of combustible mixtures. *Plasma Sources*

Table A2: List of reactions included in the model, with reaction rate coefficients and references. The symbol M denotes a neutral molecule (either N_2 or O_2). Reaction rate coefficients are in units of $cm^3\,s^{-1}$ and $cm^6\,s^{-1}$ for two-body and three-body reactions, respectively. Reaction rate coefficients for reactions R1–R30 are functions of the reduced electric field E/N, and they are computed with BOLSIG+ [46]. T(K) and T_e(K) are gas and electron temperatures, respectively. T_e(eV) is also a measure of electron temperature but in a unit of eV, by multiplying T_e(K) with the Boltzmann constant.

No.	Reaction	Reaction rate coefficient ($cm^3\,s^{-1}$ or $cm^6\,s^{-1}$)	Reference
(1) Rotational excitation			
R1	$e + N_2 \rightarrow e + N_2(J)$	$f_1(E/N)$	[47, 49]
R2	$e + O_2 \rightarrow e + O_2(J)$	$f_2(E/N)$	[47, 48]
(2) Vibrational excitation			
R3	$e + N_2 \rightarrow e + N_2(v_1)$	$f_3(E/N)$	[47, 49]
R4	$e + N_2 \rightarrow e + N_2(v_2)$	$f_4(E/N)$	[47, 49]
R5	$e + N_2 \rightarrow e + N_2(v_3)$	$f_5(E/N)$	[47, 49]
R6	$e + N_2 \rightarrow e + N_2(v_4)$	$f_6(E/N)$	[47, 49]
R7	$e + N_2 \rightarrow e + N_2(v_5)$	$f_7(E/N)$	[47, 49]
R8	$e + N_2 \rightarrow e + N_2(v_6)$	$f_8(E/N)$	[47, 49]
R9	$e + N_2 \rightarrow e + N_2(v_7)$	$f_9(E/N)$	[47, 49]
R10	$e + N_2 \rightarrow e + N_2(v_8)$	$f_{10}(E/N)$	[47, 49]
R11	$e + O_2 \rightarrow e + O_2(v_1)$	$f_{11}(E/N)$	[47, 48]
R12	$e + O_2 \rightarrow e + O_2(v_2)$	$f_{12}(E/N)$	[47, 48]
R13	$e + O_2 \rightarrow e + O_2(v_3)$	$f_{13}(E/N)$	[47, 48]
R14	$e + O_2 \rightarrow e + O_2(v_4)$	$f_{14}(E/N)$	[47, 48]
(3) Electron excitation			
R15	$e + N_2 \rightarrow e + N_2(A)$	$f_{15}(E/N)$	[47, 49]
R16	$e + N_2 \rightarrow e + N_2(B)$	$f_{16}(E/N)$	[47, 49]
R17	$e + N_2 \rightarrow e + N_2(a)$	$f_{17}(E/N)$	[47, 49]
R18	$e + N_2 \rightarrow e + N_2(C)$	$f_{18}(E/N)$	[47, 49]
R19	$e + N_2 \rightarrow e + N_2(E)$	$f_{19}(E/N)$	[47, 49]
R20	$e + O_2 \rightarrow e + O_2(a)$	$f_{20}(E/N)$	[47, 48]
R21	$e + O_2 \rightarrow e + O_2(b)$	$f_{21}(E/N)$	[47, 48]
R22	$e + O_2 \rightarrow e + O_2(A)$	$f_{22}(E/N)$	[47, 48]
(4) Electron dissociation			
R23	$e + N_2 \rightarrow e + N(^4S) + N(^2D)$	$f_{23}(E/N)$	[47, 49]
R24	$e + O_2 \rightarrow e + O(^3P) + O(^3P)$	$f_{24}(E/N)$	[47, 48]
R25	$e + O_2 \rightarrow e + O(^3P) + O(^1D)$	$f_{25}(E/N)$	[47, 48]
R26	$e + O_2 \rightarrow e + O(^3P) + O(^1S)$	$f_{26}(E/N)$	[47, 48]
(5) Electron impact ionization			
R27	$e + N_2 \rightarrow 2e + N_2^+$	$f_{27}(E/N)$	[47, 49]
R28	$e + O_2 \rightarrow 2e + O_2^+$	$f_{28}(E/N)$	[47, 48]
(6) Electron attachment			
R29	$e + O_2 + O_2 \rightarrow O_2^- + O_2$	$f_{29}(E/N)$	[47, 48]
R30	$e + O_2 \rightarrow O^- + O(^3P)$	$f_{30}(E/N)$	[47, 48]
R31	$e + O_2 + N_2 \rightarrow O_2^- + N_2$	1.10×10^{-31}	[26]
R32	$e + O_3 + O_2 \rightarrow O_3^- + O_2$	1.00×10^{-31}	[26]
R33	$e + O_3 \rightarrow O_2^- + O(^3P)$	1.00×10^{-9}	[19]
R34	$e + O_3 \rightarrow O^- + O_2$	1.00×10^{-11}	[19]
R35	$e + NO + M \rightarrow NO^- + M$	1.00×10^{-30}	[19]
R36	$e + NO_2(+M) \rightarrow NO_2^-(+M)$	3.00×10^{-11}	[19]
R37	$e + NO_2 \rightarrow O^- + NO$	1.00×10^{-11}	[19]
R38	$e + N_2O + N_2 \rightarrow N_2O^- + N_2$	$(4.72(T_e(\mathrm{eV}) + 0.412)^2 - 1.268) \times 10^{-31}$	[19]
R39	$e + O(^3P) + O_2 \rightarrow O_2^- + O(^3P)$	1.00×10^{-31}	[19]
R40	$e + O(^3P) + O_2 \rightarrow O^- + O_2$	1.00×10^{-31}	[19]
R41	$e + O(^3P) + N_2 \rightarrow O^- + N_2$	1.00×10^{-31}	[26]

Table A2: (Continued from previous page)

No.	Reaction	Reaction rate coefficient ($cm^3\,s^{-1}$ or $cm^6\,s^{-1}$)	Reference
(7) Electron detachment			
R42	$O^- + O_2 \rightarrow e + O_3$	5.00×10^{-15}	[19]
R43	$O^- + O_2(a) \rightarrow e + O_3$	3.00×10^{-10}	[19]
R44	$O^- + O_2(b) \rightarrow e + O_2 + O(^3P)$	6.90×10^{-10}	[19]
R45	$O^- + O_3 \rightarrow e + 2O_2$	5.30×10^{-10}	[26]
R46	$O^- + N_2 \rightarrow e + N_2O$	$1.16 \times 10^{-12} \exp(-(\frac{48.9}{11+E/N})^2)$	[28]
R47	$O^- + N_2(A) \rightarrow e + N_2 + O(^3P)$	2.20×10^{-9}	[19]
R48	$O^- + N_2(B) \rightarrow e + N_2 + O(^3P)$	1.90×10^{-9}	[19]
R49	$O^- + NO \rightarrow e + NO_2$	2.60×10^{-10}	[19]
R50	$O^- + O(^3P) \rightarrow e + O_2$	5.00×10^{-10}	[19]
R51	$O^- + N(^4S) \rightarrow e + NO$	2.60×10^{-10}	[19]
R52	$O_2^- + M \rightarrow e + O_2 + M$	$1.24 \times 10^{-11} \exp(-(\frac{179}{8.8+E/N})^2)$	[28]
R53	$O_2^- + O_2(a) \rightarrow e + 2O_2$	2.00×10^{-10}	[19]
R54	$O_2^- + O_2(b) \rightarrow e + 2O_2$	3.60×10^{-10}	[19]
R55	$O_2^- + N_2(A) \rightarrow e + O_2 + N_2$	2.10×10^{-9}	[19]
R56	$O_2^- + N_2(B) \rightarrow e + O_2 + N_2$	2.50×10^{-9}	[19]
R57	$O_2^- + O(^3P) \rightarrow e + O_3$	1.50×10^{-10}	[19]
R58	$O_2^- + N(^4S) \rightarrow e + NO_2$	5.00×10^{-10}	[19]
R59	$O_3^- + O_3 \rightarrow e + 3O_2$	1.00×10^{-10}	[26]
R60	$O_3^- + O(^3P) \rightarrow e + 2O_2$	3.00×10^{-10}	[19]
(8) Negative ion conversion			
R61	$O^- + O_2 + M \rightarrow O_3^- + M$	$1.10 \times 10^{-30} \exp(-(\frac{E/N}{65})^2)$	[28]
R62	$O^- + O_2 \rightarrow O_2^- + O(^3P)$	$6.96 \times 10^{-11} \exp(-(\frac{198}{5.6+E/N})^2)$	[28]
R63	$O^- + O_2(a) \rightarrow O_2^- + O(^3P)$	1.00×10^{-10}	[19]
R64	$O^- + O_3 \rightarrow O_3^- + O(^3P)$	5.30×10^{-10}	[19]
R65	$O^- + NO + M \rightarrow NO_2^- + M$	1.00×10^{-29}	[19]
R66	$O^- + NO_2 \rightarrow NO_2^- + O(^3P)$	1.20×10^{-9}	[19]
R67	$O^- + N_2O \rightarrow NO^- + NO$	2.00×10^{-10}	[19]
R68	$O^- + N_2O \rightarrow N_2O^- + O(^3P)$	2.00×10^{-12}	[19]
R69	$O_2^- + O_2 + M \rightarrow O_4^- + M$	$3.50 \times 10^{-31} (\frac{300}{T})$	[19]
R70	$O_2^- + O_3 \rightarrow O_3^- + O_2$	4.00×10^{-10}	[19]
R71	$O_2^- + NO_2 \rightarrow NO_2^- + O_2$	8.00×10^{-10}	[19]
R72	$O_2^- + NO_3 \rightarrow NO_3^- + O_2$	5.00×10^{-10}	[19]
R73	$O_2^- + N_2O \rightarrow O_3^- + N_2$	1.00×10^{-12}	[19]
R74	$O_2^- + O(^3P) \rightarrow O^- + O_2$	3.30×10^{-10}	[19]
R75	$O_3^- + NO \rightarrow NO_2^- + O_2$	2.60×10^{-12}	[19]
R76	$O_3^- + NO \rightarrow NO_3^- + O(^3P)$	1.00×10^{-11}	[19]
R77	$O_3^- + NO_2 \rightarrow NO_2^- + O_3$	7.00×10^{-10}	[19]
R78	$O_3^- + NO_2 \rightarrow NO_3^- + O_2$	2.00×10^{-11}	[19]
R79	$O_3^- + NO_3 \rightarrow NO_3^- + O_3$	5.00×10^{-10}	[19]
R80	$O_3^- + O(^3P) \rightarrow O_2^- + O_2$	3.20×10^{-10}	[19]
R81	$O_4^- + M \rightarrow O_2^- + O_2 + M$	$1.00 \times 10^{-10} \exp(\frac{-1044}{T})$	[19]
R82	$O_4^- + O_2(a) \rightarrow O_2^- + 2O_2$	1.00×10^{-10}	[19]
R83	$O_4^- + O_2(b) \rightarrow O_2^- + 2O_2$	1.00×10^{-10}	[19]
R84	$O_4^- + NO \rightarrow NO_3^- + O_2$	2.50×10^{-10}	[19]
R85	$O_4^- + O(^3P) \rightarrow O^- + 2O_2$	3.00×10^{-10}	[19]
R86	$O_4^- + O(^3P) \rightarrow O_3^- + O_2$	4.00×10^{-10}	[19]
(9) Positive ion conversion			
R87	$N_2^+ + O_2 \rightarrow O_2^+ + N_2$	$6.00 \times 10^{-11} (\frac{300}{T})^{0.5}$	[19]
R88	$N_2^+ + O_3 \rightarrow O_2^+ + N_2 + O(^3P)$	1.00×10^{-10}	[19]
R89	$N_2^+ + N_2 + M \rightarrow N_4^+ + M$	$5.00 \times 10^{-29} (\frac{300}{T})^2$	[19, 21]
R90	$N_2^+ + N_2(A) \rightarrow N_3^+ + N(^4S)$	3.00×10^{-10}	[19]
R91	$N_2^+ + NO \rightarrow NO^+ + N_2$	3.30×10^{-10}	[19]
R92	$N_2^+ + NO_2 \rightarrow NO_2^+ + N_2$	3.00×10^{-10}	[23]
R93	$N_2^+ + N_2O \rightarrow NO^+ + N_2 + N(^4S)$	4.00×10^{-10}	[19]
R94	$N_2^+ + N_2O \rightarrow N_2O^+ + N_2$	5.00×10^{-10}	[19]

Table A2: (Continued from previous page)

No.	Reaction	Reaction rate coefficient ($cm^3\,s^{-1}$ or $cm^6\,s^{-1}$)	Reference
R95	$N_2^+ + O(^3P) \rightarrow O^+ + N_2$	$1.00 \times 10^{-11}(\frac{300}{T})^{0.2}$	[19]
R96	$N_2^+ + O(^3P) \rightarrow NO^+ + N(^4S)$	$1.30 \times 10^{-10}(\frac{300}{T})^{0.5}$	[19]
R97	$N_2^+ + N(^4S) + M \rightarrow N_3^+ + M$	$9.00 \times 10^{-30}\exp(\frac{400}{T})$	[19, 21]
R98	$N_2^+ + N(^4S) \rightarrow N^+ + N_2$	$2.40 \times 10^{-15}T$	[19]
R99	$N_4^+ + O_2 \rightarrow O_2^+ + 2N_2$	2.50×10^{-10}	[19]
R100	$N_4^+ + N_2 \rightarrow N_2^+ + 2N_2$	$10^{-14.6+0.0036(T-300)}$	[19]
R101	$N_4^+ + NO \rightarrow NO^+ + 2N_2$	4.00×10^{-10}	[19]
R102	$N_4^+ + O(^3P) \rightarrow O^+ + 2N_2$	2.50×10^{-10}	[19]
R103	$N_4^+ + N(^4S) \rightarrow N^+ + 2N_2$	1.00×10^{-11}	[19]
R104	$O_2^+ + O_2 + M \rightarrow O_4^+ + M$	$2.40 \times 10^{-30}(\frac{300}{T})^3$	[19, 21]
R105	$O_2^+ + N_2 + N_2 \rightarrow N_2O_2^+ + N_2$	$9.00 \times 10^{-31}(\frac{300}{T})^2$	[19]
R106	$O_2^+ + N_2 \rightarrow NO^+ + NO$	1.00×10^{-17}	[19]
R107	$O_2^+ + NO \rightarrow NO^+ + O_2$	4.40×10^{-10}	[19]
R108	$O_2^+ + NO_2 \rightarrow NO^+ + O_3$	1.00×10^{-11}	[19]
R109	$O_2^+ + NO_2 \rightarrow NO_2^+ + O_2$	6.60×10^{-10}	[19]
R110	$O_2^+ + N(^4S) \rightarrow NO^+ + O(^3P)$	1.20×10^{-10}	[19]
R111	$O_4^+ + O_2 \rightarrow O_2^+ + 2O_2$	$3.30 \times 10^{-6}(\frac{300}{T})^4\exp(\frac{-5030}{T})$	[19]
R112	$O_4^+ + O_2(a) \rightarrow O_2^+ + 2O_2$	1.00×10^{-10}	[19]
R113	$O_4^+ + O_2(b) \rightarrow O_2^+ + 2O_2$	1.00×10^{-10}	[19]
R114	$O_4^+ + N_2 \rightarrow N_2O_2^+ + O_2$	$4.61 \times 10^{-12}(\frac{T}{300})^{2.5}\exp(\frac{-2650}{T})$	[19]
R115	$O_4^+ + NO \rightarrow NO^+ + 2O_2$	1.00×10^{-10}	[19]
R116	$O_4^+ + NO_2 \rightarrow NO_2^+ + 2O_2$	3.00×10^{-10}	[23]
R117	$O_4^+ + O(^3P) \rightarrow O_2^+ + O_3$	3.00×10^{-10}	[19]
R118	$N_2O_2^+ + O_2 \rightarrow O_4^+ + N_2$	1.00×10^{-9}	[19]
R119	$N_2O_2^+ + N_2 \rightarrow O_2^+ + 2N_2$	$1.10 \times 10^{-6}(\frac{300}{T})^{5.3}\exp(\frac{-2357}{T})$	[19]
(10) Electron-ion recombination			
R120	$e + N_2^+ + M \rightarrow N_2 + M$	$6.00 \times 10^{-27}(\frac{300}{T_e})^{1.5}$	[19]
R121	$e + N_2^+ \rightarrow N(^4S) + N(^4S)$	$2.80 \times 10^{-7}(\frac{300}{T_e})^{0.5}$	[19, 25]
R122	$e + N_2^+ \rightarrow N(^4S) + N(^2D)$	$2.00 \times 10^{-7}(\frac{300}{T_e})^{0.5}$	[19]
R123	$e + N_4^+ \rightarrow 2N_2$	$2.00 \times 10^{-6}(\frac{300}{T_e})^{0.5}$	[19]
R124	$e + O_2^+ + M \rightarrow O_2 + M$	$6.00 \times 10^{-27}(\frac{300}{T_e})^{1.5}$	[19]
R125	$e + O_2^+ \rightarrow O(^3P) + O(^1D)$	$1.95 \times 10^{-7}(\frac{300}{T_e})^{0.7}$	[19, 25]
R126	$e + O_4^+ \rightarrow 2O_2$	$1.40 \times 10^{-6}(\frac{300}{T_e})^{0.5}$	[19]
R127	$e + N_2O_2^+ \rightarrow N_2 + O_2$	$1.30 \times 10^{-6}(\frac{300}{T_e})^{0.5}$	[19]
(11) Ion-ion recombination			
R128	$N_2^+ + O^- + M \rightarrow N_2O + M$	$2.00 \times 10^{-25}(\frac{300}{T})^{2.5}$	[19]
R129	$N_2^+ + O^- + M \rightarrow N_2 + O(^3P) + M$	$2.00 \times 10^{-25}(\frac{300}{T})^{2.5}$	[19]
R130	$N_2^+ + O^- \rightarrow N_2 + O(^3P)$	$2.00 \times 10^{-7}(\frac{300}{T})^{0.5}$	[19]
R131	$N_2^+ + O^- \rightarrow 2N(^4S) + O(^3P)$	1.00×10^{-7}	[19]
R132	$N_2^+ + O_2^- + M \rightarrow N_2 + O_2 + M$	$2.00 \times 10^{-25}(\frac{300}{T})^{2.5}$	[19]
R133	$N_2^+ + O_2^- \rightarrow N_2 + O_2$	$2.00 \times 10^{-7}(\frac{300}{T})^{0.5}$	[19]
R134	$N_2^+ + O_2^- \rightarrow O_2 + 2N(^4S)$	1.00×10^{-7}	[19]
R135	$N_2^+ + O_3^- \rightarrow N_2 + O_3$	$2.00 \times 10^{-7}(\frac{300}{T})^{0.5}$	[19]
R136	$N_2^+ + O_3^- \rightarrow O_3 + 2N(^4S)$	1.00×10^{-7}	[19]
R137	$N_2^+ + O_4^- \rightarrow N_2 + 2O_2$	1.00×10^{-7}	[19]
R138	$N_4^+ + O^- \rightarrow 2N_2 + O(^3P)$	1.00×10^{-7}	[19]
R139	$N_4^+ + O_2^- \rightarrow 2N_2 + O_2$	1.00×10^{-7}	[19]
R140	$N_4^+ + O_3^- \rightarrow 2N_2 + O_3$	1.00×10^{-7}	[19]
R141	$N_4^+ + O_4^- \rightarrow 2N_2 + 2O_2$	1.00×10^{-7}	[19]
R142	$O_2^+ + O^- + M \rightarrow O_3 + M$	$2.00 \times 10^{-25}(\frac{300}{T})^{2.5}$	[19]
R143	$O_2^+ + O^- + M \rightarrow O_2 + O(^3P) + M$	$2.00 \times 10^{-25}(\frac{300}{T})^{2.5}$	[19]
R144	$O_2^+ + O^- \rightarrow O_2 + O(^3P)$	$2.00 \times 10^{-7}(\frac{300}{T})^{0.5}$	[19]
R145	$O_2^+ + O^- \rightarrow 3O(^3P)$	1.00×10^{-7}	[19]
R146	$O_2^+ + O_2^- + M \rightarrow 2O_2 + M$	$2.00 \times 10^{-25}(\frac{300}{T})^{2.5}$	[19]
R147	$O_2^+ + O_2^- \rightarrow 2O_2$	$2.00 \times 10^{-7}(\frac{300}{T})^{0.5}$	[19]
R148	$O_2^+ + O_2^- \rightarrow O_2 + 2O(^3P)$	1.00×10^{-7}	[19]

Table A2: (Continued from previous page)

No.	Reaction	Reaction rate coefficient ($cm^3\,s^{-1}$ or $cm^6\,s^{-1}$)	Reference
R149	$O_2^+ + O_3^- \rightarrow O_2 + O_3$	$2.00 \times 10^{-7}(\frac{300}{T})^{0.5}$	[19]
R150	$O_2^+ + O_3^- \rightarrow O_3 + 2O(^3P)$	1.00×10^{-7}	[19]
R151	$O_2^+ + O_4^- \rightarrow 3O_2$	1.00×10^{-7}	[19]
R152	$O_4^+ + O^- \rightarrow 2O_2 + O(^3P)$	1.00×10^{-7}	[19]
R153	$O_4^+ + O_2^- \rightarrow 3O_2$	1.00×10^{-7}	[19]
R154	$O_4^+ + O_3^- \rightarrow 2O_2 + O_3$	1.00×10^{-7}	[19]
R155	$O_4^+ + O_4^- \rightarrow 4O_2$	1.00×10^{-7}	[19]
R156	$N_2O_2^+ + O^- \rightarrow N_2 + O_2 + O(^3P)$	1.00×10^{-7}	[19]
R157	$N_2O_2^+ + O^- \rightarrow 2NO + O(^3P)$	1.00×10^{-7}	[26]
R158	$N_2O_2^+ + O_2^- \rightarrow N_2 + 2O_2$	1.00×10^{-7}	[19]
R159	$N_2O_2^+ + O_2^- \rightarrow 2NO + O_2$	1.00×10^{-7}	[26]
R160	$N_2O_2^+ + O_3^- \rightarrow N_2 + O_2 + O_3$	1.00×10^{-7}	[19]
R161	$N_2O_2^+ + O_3^- \rightarrow 2NO + O_3$	1.00×10^{-7}	[26]
R162	$N_2O_2^+ + O_4^- \rightarrow N_2 + 3O_2$	1.00×10^{-7}	[19]
(12) Neutral species conversion			
R163	$N_2(A) + O_2 \rightarrow N_2 + O_2(a)$	5.40×10^{-13}	[19, 27]
R164	$N_2(A) + O_2 \rightarrow N_2 + O_2(b)$	7.50×10^{-13}	[27]
R165	$N_2(A) + O_2 \rightarrow N_2 + 2O(^3P)$	2.54×10^{-12}	[19]
R166	$N_2(A) + O_2 \rightarrow N_2O + O(^3P)$	7.80×10^{-14}	[19]
R167	$N_2(A) + N_2 \rightarrow 2N_2$	3.00×10^{-18}	[19]
R168	$N_2(A) + N_2(A) \rightarrow N_2 + N_2(B)$	7.70×10^{-11}	[27]
R169	$N_2(A) + N_2(A) \rightarrow N_2 + N_2(C)$	1.60×10^{-10}	[19]
R170	$N_2(A) + NO \rightarrow N_2 + NO$	7.00×10^{-11}	[19]
R171	$N_2(A) + N_2O \rightarrow N_2 + NO + N(^4S)$	1.00×10^{-11}	[19]
R172	$N_2(A) + O(^3P) \rightarrow N_2 + O(^1S)$	2.10×10^{-11}	[19]
R173	$N_2(A) + O(^3P) \rightarrow NO + N(^2D)$	7.00×10^{-12}	[19]
R174	$N_2(A) + N(^4S) \rightarrow N_2 + N(^4S)$	2.00×10^{-12}	[20]
R175	$N_2(A) + N(^4S) \rightarrow N_2 + N(^2P)$	5.00×10^{-11}	[19]
R176	$N_2(B) + O_2 \rightarrow N_2 + 2O(^3P)$	3.00×10^{-10}	[19]
R177	$N_2(B) + N_2 \rightarrow 2N_2$	2.00×10^{-12}	[26]
R178	$N_2(B) + N_2 \rightarrow N_2 + N_2(A)$	5.00×10^{-11}	[19]
R179	$N_2(B) + NO \rightarrow NO + N_2(A)$	2.40×10^{-10}	[19]
R180	$N_2(B) \rightarrow N_2(A) + h\nu$	1.50×10^5 (s^{-1})	[19]
R181	$N_2(a) + O_2 \rightarrow N_2 + O(^3P) + O(^3P)$	2.80×10^{-11}	[19]
R182	$N_2(a) + N_2 \rightarrow N_2 + N_2(B)$	2.00×10^{-13}	[19]
R183	$N_2(a) + NO \rightarrow N_2 + N(^4S) + O(^3P)$	3.60×10^{-10}	[19]
R184	$N_2(C) + O_2 \rightarrow N_2 + O(^3P) + O(^1S)$	3.00×10^{-10}	[19]
R185	$N_2(C) + N_2 \rightarrow N_2 + N_2(a)$	1.00×10^{-11}	[19]
R186	$N_2(C) \rightarrow N_2(B) + h\nu$	3.00×10^7 (s^{-1})	[19]
R187	$N_2(E) + N_2 \rightarrow N_2 + N_2(C)$	1.00×10^{-11}	[22]
R188	$N(^4S) + O_2 \rightarrow NO + O(^3P)$	$4.50 \times 10^{-12}\exp(\frac{-3220}{T})$	[19]
R189	$N(^4S) + O_3 \rightarrow NO + O_2$	2.00×10^{-16}	[19]
R190	$N(^4S) + NO \rightarrow N_2 + O(^3P)$	$1.05 \times 10^{-12}T^{0.5}$	[19]
R191	$N(^4S) + NO_2 \rightarrow N_2 + O_2$	7.00×10^{-13}	[19]
R192	$N(^4S) + NO_2 \rightarrow N_2 + 2O(^3P)$	9.10×10^{-13}	[19]
R193	$N(^4S) + NO_2 \rightarrow 2NO$	2.30×10^{-12}	[19]
R194	$N(^4S) + NO_2 \rightarrow N_2O + O(^3P)$	3.00×10^{-12}	[19]
R195	$N(^4S) + O(^3P) + M \rightarrow NO + M$	$1.76 \times 10^{-31}T^{-0.5}$	[19]
R196	$N(^4S) + N(^4S) + M \rightarrow N_2 + M$	$8.27 \times 10^{-34}\exp(\frac{500}{T})$	[19]
R197	$N(^4S) + N(^2P) \rightarrow N(^4S) + N(^2D)$	1.80×10^{-12}	[19]
R198	$N(^2D) + O_2 \rightarrow NO + O(^3P)$	$1.50 \times 10^{-12}(\frac{T}{300})^{0.5}$	[19]
R199	$N(^2D) + O_2 \rightarrow NO + O(^1D)$	$6.00 \times 10^{-12}(\frac{T}{300})^{0.5}$	[19]
R200	$N(^2D) + N_2 \rightarrow N_2 + N(^4S)$	6.00×10^{-15}	[19]
R201	$N(^2D) + NO(+M) \rightarrow N_2O(+M)$	6.00×10^{-11}	[19]
R202	$N(^2D) + N_2O \rightarrow NO + N_2$	3.00×10^{-12}	[19]
R203	$N(^2P) + O_2 \rightarrow NO + O(^3P)$	2.60×10^{-12}	[19]
R204	$N(^2P) + N_2 \rightarrow N_2 + N(^2D)$	2.00×10^{-18}	[19]
R205	$N(^2P) + NO \rightarrow N_2(A) + O(^3P)$	3.40×10^{-11}	[19]

Table A2: (Continued from previous page)

No.	Reaction	Reaction rate coefficient ($cm^3\,s^{-1}$ or $cm^6\,s^{-1}$)	Reference
R206	$O_2(a) + O_2 \rightarrow 2O_2$	$2.20 \times 10^{-18}(\frac{T}{300})^{0.8}$	[19]
R207	$O_2(a) + O_2(a) + O_2 \rightarrow 2O_3$	1.00×10^{-31}	[20]
R208	$O_2(a) + O_2(a) \rightarrow O_2 + O_2(b)$	$7.00 \times 10^{-28} T^{3.8} \exp(\frac{700}{T})$	[20]
R209	$O_2(a) + O_3 \rightarrow 2O_2 + O(^3P)$	$9.70 \times 10^{-13} \exp(\frac{-1564}{T})$	[19]
R210	$O_2(a) + N_2 \rightarrow O_2 + N_2$	3.00×10^{-21}	[19]
R211	$O_2(a) + NO \rightarrow NO + O_2$	2.50×10^{-11}	[19]
R212	$O_2(a) + O(^3P) \rightarrow O_2 + O(^3P)$	7.00×10^{-16}	[19]
R213	$O_2(a) + O(^1S) \rightarrow 3O(^3P)$	3.40×10^{-11}	[19]
R214	$O_2(a) + O(^1S) \rightarrow O_2(b) + O(^1D)$	3.60×10^{-11}	[19]
R215	$O_2(a) + O(^1S) \rightarrow O_2(A) + O(^3P)$	1.30×10^{-10}	[19]
R216	$O_2(a) + N(^4S) \rightarrow NO + O(^3P)$	$2.00 \times 10^{-14} \exp(\frac{-600}{T})$	[19]
R217	$O_2(b) + O_2 \rightarrow O_2 + O_2(a)$	$4.30 \times 10^{-22} T^{2.4} \exp(\frac{-241}{T})$	[19]
R218	$O_2(b) + O_3 \rightarrow 2O_2 + O(^3P)$	1.80×10^{-11}	[19]
R219	$O_2(b) + N_2 \rightarrow N_2 + O_2(a)$	$4.90 \times 10^{-15} \exp(\frac{-253}{T})$	[19]
R220	$O_2(b) + NO \rightarrow NO + O_2(a)$	4.00×10^{-14}	[19]
R221	$O_2(b) + O(^3P) \rightarrow O_2(a) + O(^3P)$	8.00×10^{-14}	[19]
R222	$O_2(b) + O(^3P) \rightarrow O_2 + O(^1D)$	$3.39 \times 10^{-11}(\frac{300}{T})^{0.1} \exp(\frac{-4201}{T})$	[19]
R223	$O_2(A) + O_2 \rightarrow 2O_2(b)$	2.90×10^{-13}	[19]
R224	$O_2(A) + N_2 \rightarrow N_2 + O_2(b)$	3.00×10^{-13}	[19]
R225	$O_2(A) + O(^3P) \rightarrow O_2(b) + O(^1D)$	9.00×10^{-12}	[19]
R226	$O(^3P) + O_2 + O_2 \rightarrow O_3 + O_2$	$6.90 \times 10^{-34}(\frac{300}{T})^{1.25}$	[19]
R227	$O(^3P) + O_2 + N_2 \rightarrow O_3 + N_2$	$6.20 \times 10^{-34}(\frac{300}{T})^{2}$	[19]
R228	$O(^3P) + O_3 \rightarrow 2O_2$	$2.00 \times 10^{-11} \exp(\frac{-2300}{T})$	[19]
R229	$O(^3P) + NO + O_2 \rightarrow NO_2 + O_2$	$9.30 \times 10^{-32}(\frac{300}{T})^{1.682}$	[26]
R230	$O(^3P) + NO + N_2 \rightarrow NO_2 + N_2$	$1.20 \times 10^{-31}(\frac{300}{T})^{1.682}$	[26]
R231	$O(^3P) + NO_2 + M \rightarrow NO_3 + M$	$8.90 \times 10^{-32}(\frac{300}{T})^{2}$	[26]
R232	$O(^3P) + NO_2 \rightarrow NO + O_2$	$1.13 \times 10^{-11}(\frac{T}{1000})^{0.18}$	[19]
R233	$O(^3P) + NO_3 \rightarrow NO_2 + O_2$	1.00×10^{-11}	[19]
R234	$O(^3P) + O(^3P) + O_2 \rightarrow 2O_2$	$2.45 \times 10^{-31} T^{-0.63}$	[19]
R235	$O(^3P) + O(^3P) + N_2 \rightarrow O_2 + N_2$	$2.76 \times 10^{-34} \exp(\frac{720}{T})$	[19]
R236	$O(^3P) + O(^1S) \rightarrow O(^3P) + O(^1D)$	$5.00 \times 10^{-11} \exp(\frac{-301}{T})$	[19]
R237	$O(^1D) + O_2 \rightarrow O_2 + O(^3P)$	$6.40 \times 10^{-12} \exp(\frac{67}{T})$	[19]
R238	$O(^1D) + O_2 \rightarrow O_2(b) + O(^3P)$	$2.56 \times 10^{-11} \exp(\frac{67}{T})$	[19]
R239	$O(^1D) + O_3 \rightarrow 2O_2$	1.20×10^{-10}	[19]
R240	$O(^1D) + O_3 \rightarrow O_2 + 2O(^3P)$	1.20×10^{-10}	[19]
R241	$O(^1D) + N_2 \rightarrow N_2 + O(^3P)$	$1.80 \times 10^{-11} \exp(\frac{107}{T})$	[19]
R242	$O(^1D) + NO \rightarrow O_2 + N(^4S)$	1.70×10^{-10}	[19]
R243	$O(^1D) + NO_2 \rightarrow NO + O_2$	3.00×10^{-10}	[26]
R244	$O(^1D) + N_2O \rightarrow N_2 + O_2$	4.40×10^{-11}	[19]
R245	$O(^1D) + N_2O \rightarrow 2NO$	7.20×10^{-11}	[19]
R246	$O(^1S) + O_2 \rightarrow O_2 + O(^1D)$	$1.33 \times 10^{-12} \exp(\frac{-850}{T})$	[19]
R247	$O(^1S) + O_2 \rightarrow O_2(A) + O(^3P)$	$2.97 \times 10^{-12} \exp(\frac{-850}{T})$	[19]
R248	$O(^1S) + O_3 \rightarrow 2O_2$	2.90×10^{-10}	[19]
R249	$O(^1S) + O_3 \rightarrow O_2 + O(^3P) + O(^1D)$	2.90×10^{-10}	[19]
R250	$O(^1S) + NO \rightarrow NO + O(^3P)$	1.80×10^{-10}	[19]
R251	$O(^1S) + NO \rightarrow NO + O(^1D)$	3.20×10^{-10}	[19]
R252	$O(^1S) + N_2O \rightarrow N_2O + O(^3P)$	6.30×10^{-12}	[19]
R253	$O(^1S) + N_2O \rightarrow N_2O + O(^1D)$	3.10×10^{-12}	[19]
R254	$NO + O_3 \rightarrow NO_2 + O_2$	$4.30 \times 10^{-12} \exp(\frac{-1560}{T})$	[19]
R255	$NO + NO + O_2 \rightarrow 2NO_2$	$3.30 \times 10^{-39} \exp(\frac{530}{T})$	[24]
R256	$NO + NO_2 + N_2 \rightarrow N_2O_3 + N_2$	$3.10 \times 10^{-34}(\frac{300}{T})^{7.7}$	[24]
R257	$NO + NO_2 + NO_3 \rightarrow NO + N_2O_5$	$5.90 \times 10^{-29}(\frac{300}{T})^{1.27}$	[26]
R258	$NO + NO_3 \rightarrow 2NO_2$	1.70×10^{-11}	[19]
R259	$NO_2 + O_3 \rightarrow NO_3 + O_2$	$1.20 \times 10^{-13} \exp(\frac{-2450}{T})$	[19]
R260	$NO_2 + NO_2 + N_2 \rightarrow N_2O_4 + N_2$	$1.40 \times 10^{-33}(\frac{300}{T})^{3.8}$	[24]
R261	$NO_2 + NO_3 + M \rightarrow N_2O_5 + M$	$5.90 \times 10^{-29}(\frac{300}{T})^{1.27}$	[26]
R262	$NO_2 + NO_3 \rightarrow NO + NO_2 + O_2$	$2.30 \times 10^{-13} \exp(\frac{-1600}{T})$	[19]
R263	$NO_3 + NO_3 \rightarrow 2NO_2 + O_2$	$5.00 \times 10^{-12} \exp(\frac{-3000}{T})$	[19]

Science and Technology, 25(4):043002, August 2016.

[19] I A Kossyi, A Yu Kostinsky, A A Matveyev, and V P Silakov. Kinetic scheme of the non-equilibrium discharge in nitrogen-oxygen mixtures. *Plasma Sources Science and Technology*, 1(3):207–220, August 1992.

[20] B.F. Gordiets, C.M. Ferreira, V.L. Guerra, J.M.A.H. Loureiro, J. Nahorny, D. Pagnon, M. Touzeau, and M. Vialle. Kinetic model of a low-pressure N_2-O_2 flowing glow discharge. *IEEE Transactions on Plasma Science*, 23(4):750–768, August 1995.

[21] N L Aleksandrov and E M Bazelyan. Ionization processes in spark discharge plasmas. *Plasma Sources Science and Technology*, 8(2):285–294, May 1999.

[22] F Fresnet, G Baravian, L Magne, S Pasquiers, C Postel, V Puech, and A Rousseau. Influence of water on NO removal by pulsed discharge in $N_2/H_2O/NO$ mixtures. *Plasma Sources Science and Technology*, 11(2):152–160, May 2002.

[23] Fumiyoshi Tochikubo and Hideyuki Arai. Numerical Simulation of Streamer Propagation and Radical Reactions in Positive Corona Discharge in N_2/NO and $N_2/O_2/NO$. *Japanese Journal of Applied Physics*, 41(Part 1, No. 2A):844–852, February 2002.

[24] R. Atkinson, D. L. Baulch, R. A. Cox, J. N. Crowley, R. F. Hampson, R. G. Hynes, M. E. Jenkin, M. J. Rossi, and J. Troe. Evaluated kinetic and photochemical data for atmospheric chemistry: Volume I - gas phase reactions of O_x, HO_x, NO_x and SO_x species. *Atmospheric Chemistry and Physics*, 4(6):1461–1738, September 2004.

[25] A Florescumitchell and J Mitchell. Dissociative recombination. *Physics Reports*, 430(5-6):277–374, August 2006.

[26] F J Gordillo-Vázquez. Air plasma kinetics under the influence of sprites. *Journal of Physics D: Applied Physics*, 41(23):234016, December 2008.

[27] N A Popov. Fast gas heating in a nitrogen–oxygen discharge plasma: I. Kinetic mechanism. *Journal of Physics D: Applied Physics*, 44(28):285201, July 2011.

[28] Sergey Pancheshnyi. Effective ionization rate in nitrogen–oxygen mixtures. *Journal of Physics D: Applied Physics*, 46(15):155201, April 2013.

[29] Ryo Ono and Atsushi Komuro. Generation of the single-filament pulsed positive streamer discharge in atmospheric-pressure air and its comparison with two-dimensional simulation. *Journal of Physics D: Applied Physics*, 53(3):035202, January 2020.

[30] Dennis Bouwman, Jannis Teunissen, and Ute Ebert. 3D particle simulations of positive air–methane streamers for combustion. *Plasma Sources Science and Technology*, 31(4):045023, April 2022.

[31] Atsushi Komuro, Kazunori Takahashi, and Akira Ando. Numerical simulation for the production of chemically active species in primary and secondary streamers in atmospheric-pressure dry air. *Journal of Physics D: Applied Physics*, 48(21):215203, June 2015.

[32] G V Naidis. Modelling of plasma chemical processes in pulsed corona discharges. *Journal of Physics D: Applied Physics*, 30(8):1214–1218, April 1997.

[33] G V Naidis. Efficiency of generation of chemically active species by pulsed corona discharges. *Plasma Sources Science and Technology*, 21(4):042001, August 2012.

[34] E. M. van Veldhuizen, W. R. Rutgers, and V. A. Bityurin. Energy efficiency of NO removal by pulsed corona discharges. *Plasma Chemistry and Plasma Processing*, 16(2):227–247, June 1996.

[35] T. Namihira, S. Tsukamoto, Douyan Wang, S. Katsuki, R. Hackam, H. Akiyama, Y. Uchida, and M. Koike. Improvement of NO_x removal efficiency using short-width pulsed power. *IEEE Transactions on Plasma Science*, 28(2):434–442, April 2000.

[36] Takao Matsumoto, Douyan Wang, Takao Namihira, and Hidenori Akiyama. Energy Efficiency Improvement of Nitric Oxide Treatment Using Nanosecond Pulsed Discharge. *IEEE Transactions on Plasma Science*, 38(10):2639–2643, October 2010.

[37] Jannis Teunissen and Ute Ebert. Simulating streamer discharges in 3D with the parallel adaptive Afivo framework. *Journal of Physics D: Applied Physics*, 50(47):474001, November 2017.

[38] M B Zheleznyak, A Kh Mnatsakanyan, and S V Sizykh. Photoionization of nitrogen and oxygen mixtures by radiation from a gas discharge. *High Temperature*, 20(3):357–362, November 1982.

[39] Alejandro Luque, Ute Ebert, Carolynne Montijn, and Willem Hundsdorfer. Photoionization in negative streamers: Fast computations and two propagation modes. *Applied Physics Letters*, 90(8):081501, February 2007.

[40] A Bourdon, V P Pasko, N Y Liu, S Célestin, P Ségur, and E Marode. Efficient models for photoionization produced by non-thermal gas discharges in air based on radiative transfer and the Helmholtz equations. *Plasma Sources Science and Technology*, 16(3):656–678, August 2007.

[41] Baohong Guo, Xiaoran Li, Ute Ebert, and Jannis Teunissen. A computational study of accelerating, steady and fading negative streamers in ambient air. *Plasma Sources Science and Technology*, 31(9):095011, September 2022.

[42] Atsushi Komuro, Ryo Ono, and Tetsuji Oda. Numerical simulation for production of O and N radicals in an atmospheric-pressure streamer discharge. *Journal of Physics D: Applied Physics*, 45(26):265201, July 2012.

[43] Xiaoran Li, Baohong Guo, Anbang Sun, Ute Ebert, and Jannis Teunissen. A computational study of steady and stagnating positive streamers in N $_2$ –O $_2$ mixtures. *Plasma Sources Science and Technology*, 31(6):065011, June 2022.

[44] Jannis Teunissen and Ute Ebert. Afivo: A framework for quadtree/octree AMR with shared-memory parallelization and geometric multigrid methods. *Computer Physics Communications*, 233:156–166, December 2018.

[45] Jannis Teunissen and Francesca Schiavello. Geometric multigrid method for solving Poisson's equation on octree grids with irregular boundaries. *Computer Physics Communications*, 286:108665, May 2023.

[46] G J M Hagelaar and L C Pitchford. Solving the Boltzmann equation to obtain electron transport coefficients and rate coefficients for fluid models. *Plasma Sources Science and Technology*, 14(4):722–733, November 2005.

[47] Phelps database (N_2, O_2) `www.lxcat.net` (retrieved 8 June 2022).

[48] S. A. Lawton and A. V. Phelps. Excitation of the $b^1\Sigma_g^+$ state of O_2 by low energy electrons. *The Journal of Chemical Physics*, 69(3):1055, August 1978.

[49] A. V. Phelps and L. C. Pitchford. Anisotropic scattering of electrons by N_2 and its effect on electron transport. *Physical Review A*, 31(5):2932–2949, May 1985.

[50] Xiaoran Li, Siebe Dijcks, Sander Nijdam, Anbang Sun, Ute Ebert, and Jannis Teunissen. Comparing simulations and experiments of positive streamers in air: Steps toward model validation. *Plasma Sources Science and Technology*, 30(9):095002, September 2021.

[51] S Nijdam, G Wormeester, E M van Veldhuizen, and U Ebert. Probing background ionization: Positive streamers with varying pulse repetition rate and with a radioactive admixture. *Journal of Physics D: Applied Physics*, 44(45):455201, November 2011.

[52] Hani Francisco, Jannis Teunissen, Behnaz Bagheri, and Ute Ebert. Simulations of positive streamers in air in different electric fields: Steady motion of solitary streamer heads and the stability field. *Plasma Sources*

Science and Technology, 30(11):115007, November 2021.

[53] Alejandro Luque, Valeria Ratushnaya, and Ute Ebert. Positive and negative streamers in ambient air: Modelling evolution and velocities. *Journal of Physics D: Applied Physics*, 41(23):234005, December 2008.

[54] A Yu Starikovskiy and N L Aleksandrov. How pulse polarity and photoionization control streamer discharge development in long air gaps. *Plasma Sources Science and Technology*, 29(7):075004, July 2020.

[55] E J M van Heesch, G J J Winands, and A J M Pemen. Evaluation of pulsed streamer corona experiments to determine the O^* radical yield. *Journal of Physics D: Applied Physics*, 41(23):234015, December 2008.

[56] Ryo Ono, Yusuke Nakagawa, and Tetsuji Oda. Effect of pulse width on the production of radicals and excited species in a pulsed positive corona discharge. *Journal of Physics D: Applied Physics*, 44(48):485201, December 2011.

[57] G J J Winands, Z Liu, A J M Pemen, E J M van Heesch, K Yan, and E M van Veldhuizen. Temporal development and chemical efficiency of positive streamers in a large scale wire-plate reactor as a function of voltage waveform parameters. *Journal of Physics D: Applied Physics*, 39(14):3010–3017, July 2006.

[58] Douyan Wang, Takao Matsumoto, Takao Namihira, and Hidenori Akiyama. Development of Higher Yield Ozonizer Based on Nano-Seconds Pulsed Discharge. *Journal of Advanced Oxidation Technologies*, 13(1):71–78, January 2010.

[59] Behnaz Bagheri, Jannis Teunissen, and Ute Ebert. Simulation of positive streamers in CO_2 and in air: The role of photoionization or other electron sources. *Plasma Sources Science and Technology*, 29(12):125021, December 2020.

[60] M Šimek. Optical diagnostics of streamer discharges in atmospheric gases. *Journal of Physics D: Applied Physics*, 47(46):463001, November 2014.

[61] Atsushi Komuro, Kazunori Takahashi, and Akira Ando. Vibration-to-translation energy transfer in atmospheric-pressure streamer discharge in dry and humid air. *Plasma Sources Science and Technology*, 24(5):055020, September 2015.

[62] J. A. Guthrie, R. C. Chaney, and A. J. Cunningham. Temperature dependencies of ternary ion–molecule association reactions yielding N_3^+, N_4^+, and CO_2^+. *The Journal of Chemical Physics*, 95(2):930–936, July 1991.

[63] H. Mätzing. Chemical Kinetics of Flue Gas Cleaning by Irradiation with Electrons. In *Advances in Chemical Physics*, pages 315–402. John Wiley & Sons, Ltd, 1991.

[64] C.D. Sutherland and J. Zinn. Chemistry computations for irradiated hot air. Technical Report LA–6055-MS, 4140364, August 1975.

[65] Defense Nuclear Agency Reaction Rate Handbook, Second Edition, Revision No. 3, DNA 1948H (September 1973).